AFIT/GE/ENG/12-01


# OPTIMUM CONCENTRATION FACTOR ANALYSIS USING DYNAMIC THERMAL MODEL OF A CONCENTRATED PHOTOVOLTAIC SYSTEM

THESIS

John T. Avrett II, 2nd Lt, USAF

AFIT/GE/ENG/12-01

**DEPARTMENT OF THE AIR FORCE**
**AIR UNIVERSITY**

***AIR FORCE INSTITUTE OF TECHNOLOGY***

**Wright-Patterson Air Force Base, Ohio**

AFIT/GE/ENG/12-01

# OPTIMUM CONCENTRATION FACTOR ANALYSIS USING DYNAMIC THERMAL MODEL OF A CONCENTRATED PHOTOVOLTAIC SYSTEM

THESIS

Presented to the Faculty

Department of Electrical and Computer Engineering

Graduate School of Engineering and Management

Air Force Institute of Technology

Air University

Air Education and Training Command

In Partial Fulfillment of the Requirements for the

Degree of Master of Science in Electrical Engineering

John T. Avrett II, BS

2nd Lt, USAF

March 2012

AFIT/GE/ENG/12-01

# OPTIMUM CONCENTRATION FACTOR ANALYSIS USING DYNAMIC THERMAL MODEL OF A CONCENTRATED PHOTOVOLTAIC SYSTEM

John T. Avrett II, BS
2nd Lt, USAF

Approved:

| | |
|---|---|
| Dr. Stephen C. Cain (Chairman) | Date |
| Lt Col LaVern Starman, Ph.D (Member) | Date |
| Major Michael Pochet, Ph.D (Member) | Date |

## Abstract

Concentrated photovoltaic (PV) technology represents a growing market in the field of terrestrial solar energy production. As the demand for renewable energy technologies increases, further importance is placed upon the modeling, design, and simulation of these systems. Given the U.S. Air Force cultural shift towards energy awareness and conservation, several concentrated PV systems have been installed on Air Force installations across the country. However, there has been a dearth of research within the Air Force devoted to understanding these systems in order to possibly improve the existing technologies. This research presents a new model for a simple concentrated PV system. This model accurately determines the steady state operating temperature as a function of the concentration factor for the optical part of the concentrated PV system, in order to calculate the optimum concentration that maximizes power output and efficiency. The dynamic thermal model derived is validated experimentally using a commercial polysilicon solar cell, and is shown to accurately predict the steady state temperature and facilitates computer analysis and prediction of the ideal concentration factor.

*I dedicate these pages to Meghan, for her relentless support throughout my long academic journey. This work will not convey the magnitude of adversity that we have overcome and the abundance of fulfillment we have ahead.*

**Acknowledgements**

I would like to thank Dr. Cain for providing me the opportunity to complete this research. Dr. Cain's acute understanding of Air Force research needs has opened the door for renewable energy research at AFIT. Furthermore, Dr. Cain's insightful reviews and recommendations regarding my work has been invaluable, and I am very thankful for his patience and understanding throughout my time at AFIT.

I would also like to thank the members of my thesis committee for agreeing to review my work and preside over my defense. Without their support, this research would be in vain. I am also indebted to Dr. Terri Marsico for agreeing to review my work upon its final completion, to evaluate its applicability in the context of Air Force research and development needs.

Finally, I would like to thank my supportive family and friends for pretending to understand the content of this work. Without their uplifting head-nods and "mmhmm's" I would not have been able to stay grounded in relating this research to real world application. Trying to explain my research to you has absolutely been one of the most valuable and rewarding experiences I've had over the past year. Thank you for keeping my feet on the ground, and my head out of the clouds!

John Avrett

## Table of Contents

## List of Figures

Page

## List of Symbols

| | | | |
|---|---|---|---|
| $V_{oc}$ | *Open-circuit voltage* | $T$ | *Temperature* |
| $I_{sc}$ | *Short-circuit current* | $n_i$ | *Intrinsic carrier concentration* |
| $I_m$ | *Max operating current* | $N_D$ | *Donor concentration* |
| $V_m$ | *Max operating voltage* | $N_A$ | *Acceptor concentration* |
| $ff$ | *Fill factor* | $I_0$ | *Reverse saturation current* |
| $\eta$ | *Efficiency* | $I_D$ | *Diode current* |
| $L_n$ | *Diffusion length for electrons* | $I_{ph}$ | *Photogenerated current* |
| $L_p$ | *Diffusion length for holes* | $I_{tot}$ | *Total solar cell current* |
| $D_0$ | *Diffusion coefficient* | $n$ | *Index of refraction* |
| $\rho$ | *Resistivity* | $A$ | *Solar cell surface area* |
| $\sigma$ | *Conductivity* | $t$ | *Time* |
| $\tau$ | *Carrier lifetime* | $x$ | *One-dimensional material depth* |
| $\mu$ | *Carrier mobility* | $E$ | *Energy* |
| $\varepsilon_{sc}$ | *Relative semiconductor permittivity* | $V_{bi}$ | *Built-in voltage* |
| $E$ | *Electric Field* | $V_a$ | *Applied voltage* |
| $e$ | *Elementary charge* | $G_0$ | *Initial generation* |
| $K$ | *Boltzmann's constant* | $\alpha$ | *Absorption coefficient* |
| $I_{op}$ | *Operating current* | $h$ | *Plank's constant* |
| $V_{op}$ | *Operating voltage* | $m_e^*$ | *Effective mass of electron* |
| $R_L$ | *Load resistance (ohms)* | $m_h^*$ | *Effective mass of hole* |
| $P_{out}$ | *Output power* | $\varphi$ | *PN-junction potential* |
| $P_{in}$ | *Input power* | $E_g$ | *Band gap energy* |
| $Q$ | *Heat* | $N_c$ | *Density of states at conduction band* |
| $\lambda$ | *Wavelength* | $N_v$ | *Density of states at valence band* |
| $f$ | *Frequency* | $E_f$ | *Fermi Level* |
| $h_{plate}$ | *Isothermal Plate heat* | $E_i$ | *Intrinsic Fermi level* |
| $p$ | *Number of holes* | $x_n$ | *Depletion edge boundary on n-side* |
| $n$ | *Number of electrons* | $-x_p$ | *Depletion edge boundary on p-side* |
| $n_{po}$ | *Excess electrons on p-side* | $n_0$ | *Intrinsic concentration of electrons* |
| $p_{no}$ | *Excess holes on n-side* | $p_0$ | *Intrinsic concentration of holes* |

# OPTIMUM CONCENTRATION FACTOR ANALYSIS USING DYNAMIC THERMAL MODEL OF A CONCENTRATED PHOTOVOLTAIC SYSTEM

## I: Introduction

Energy is the key enabler to successful military operations on a global scale. To fly, fight and win in air, space, and cyberspace requires the U.S. Air Force to use vast amounts of energy. Energy is the fundamental requirement to execute every Air Force mission and the role that energy plays in successful military operations from a tactical, strategic, and operational perspective cannot be understated. As the largest consumer of energy in the Department of Defense, energy awareness within the Air Force is paramount to continued successful operations. Consequently, energy issues regarding the security and sustainable availability of this resource have created an especially acute need to evaluate energy resources in the context of military operations.

Increasingly, renewable sources of energy such as wind, solar, and hydroelectric are being evaluated for their applicability to certain military energy system requirements. Massive solar power systems have been installed on Air Force installations across the country to supplement on-base power demands. Furthermore, alternative fuels are being developed and tested in Air Force laboratories to diminish dependence upon non-renewable energy sources, so it is evident that energy issues within the Air Force prove vitally important [1]. However, in order to obtain a well-rounded objective perspective on energy issues within the Air Force, it is useful to evaluate global energy issues.

## 1.1 Global Energy Issues

Energy is a primary catalyst to development and globalization in the modern world. Furthermore, as the global population continues to increase the demand for energy will continue to rise an estimated 44 percent over the current level by 2030 [1]. A growing sector of energy production is based upon renewable energy sources such as wind, hydroelectric, and solar power. The fundamental problem with energy production today is that the majority of energy sources have a finite long-term supply. In the United States during 2009, according to the U.S. Energy Information Administration, nearly all of the electricity consumed was produced from the non-renewable fossil fuels oil, coal, and natural gas, shown below in Figure 1.

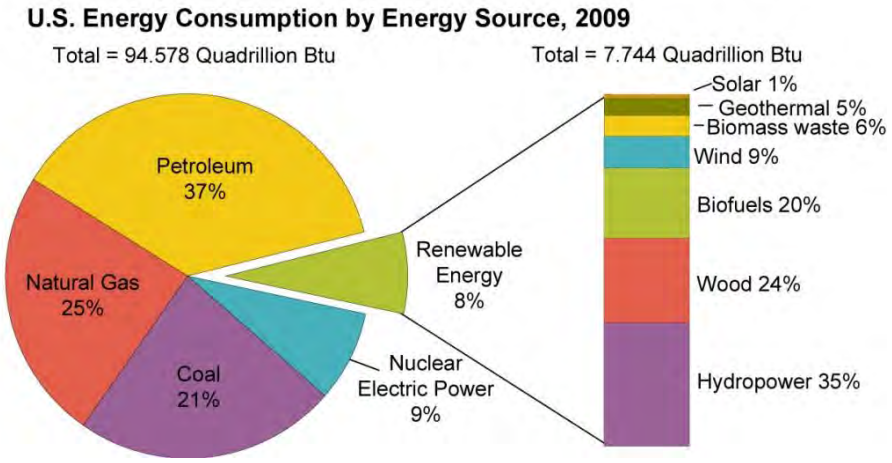


Figure 1: Global Energy Consumption [2]

As the global population continues to deplete fossil fuels from the earth, an imminent need is placed upon the exploitation and production of alternative renewable sources of energy.

The solar energy resource is one of the most promising solutions to the global energy supply problem. Every day the sun radiates to the earth roughly 10,000 times the

energy used by the global population [3]. This massive amount of energy could potentially make fossil fuel consumption obsolete in the future, but further research and development of solar energy systems is necessary to make the cost of solar energy competitive with conventional non-renewable sources of energy.

### 1.2 Air Force Energy Issues

The 2010 Air Force Energy Plan has set forth a series of energy related goals, with the primary theme "*make energy a consideration in all that we do*" [4]. Figure 2 shows the Air Force energy consumption relative to the other military service branches.

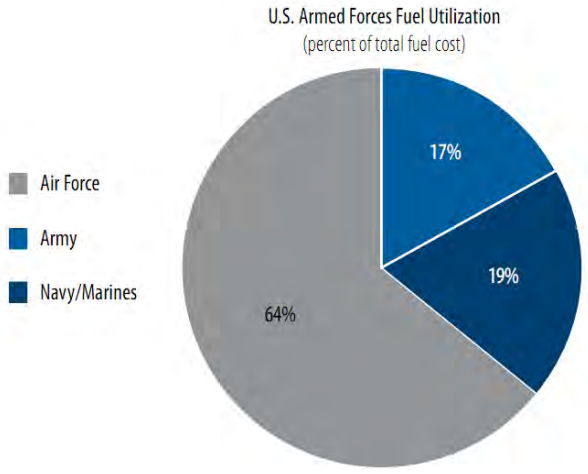


**Figure 2: Military Energy Consumption [4]**

The Air Force Energy Plan recognizes energy as an operational enabler and also demonstrates the opportunity for Air Force centric research and development of these systems. Air Force infrastructure planning, specifically, has cited the need for renewable energy systems to supplement installation energy requirements across the country [5]. Furthermore, at deployed and forward operating locations, where the raw cost of fuel does not convey the cost in manpower and logistics necessary to transport this resource in

hostile areas, the potential implementation of modular self-sustaining solar energy systems to power communications and surveillance equipment proves attractive. Engineers working on the Military Electric Project (MEP), a joint project between the U.S. Army and National Renewable Energy Lab, are currently developing a rapidly deployable solar energy system specifically for troops in forward operating locations where conventional fuel use is not appropriate [6].

The idea of energy sufficiency for troops in combat reaches far deeper than the technological details indicate. Commanders in Iraq and Afghanistan have also recognized the potential lifesaving impact that implementing renewable energy systems into combat operations could have. The conventional fuel used for generating electric power in combat is diesel fuel, which drives the generators powering most of the deployed military facilities. Since the most dangerous missions today in terms of mortality are fuel convoy missions, decreasing the number of fuel convoys necessary to meet the enormous energy demand would most certainly contribute to saving lives on the battlefield [7]. This research is motivated by the explicit need for solar energy systems in the context of Air Force operations, and covers the theoretical concepts of solar cell operation building towards a new solar cell model.

### 1.3 Solar Power Basics

The theory behind solar cell operation will be discussed comprehensively in the body of this research, but it is important to have an initial top-level understanding of solar energy systems. Solar cells generate electricity from the sun. Photons of light are absorbed to photogenerate charge carriers within the cell. The term “photovoltaic” refers

to the photovoltaic effect discovered by Alexandre-Edomond Becquerel, an experiment in which photons of light falling upon a material generate a voltage and produce a resulting current, and often times solar power systems are referred to as photovoltaic (PV) systems. While not every solar energy system uses the photovoltaic effect for energy production (such as solar thermal systems), this analysis will solely cover photovoltaic energy systems.

To generate usable amounts of power, individual solar cells are often connected in series and parallel to form solar arrays that produce power to an electrical load. Applications for PV systems range from small consumer electronics to large-scale industrial power plants generating several megawatts of power. Solar cells are also used in space-based applications to generate solar power on satellites and other space vehicles. The practical modern applications for PV systems are obvious, but as research continues and the technology is developed further, solar energy as a primary, sustainable, and reliable large-scale energy supply may become reality.

### 1.4 Concentrated Solar Power

A growing field within the photovoltaic industry is concentrated solar power (CSP). In CSP systems, parabolic mirrors or non-imaging plastic lenses focus sunlight onto the solar cell. The principle of CSP systems is that the focusing optical components increase the intensity of the sunlight on the cell relative to the degree of the focus factor of the optics, increasing the photocurrent through the cell and hence the overall power generated by the system. The immediate advantage of CSP systems is that relatively inexpensive optical components (mirrors, lenses) can be used in place of equivalent

amounts of expensive semiconductor material, thus theoretically reducing the overall cost of these systems.

Most modern CSP systems use an optical concentration ratio of up to multiple hundreds of suns [8]. Since the amount of semiconductor material necessary is relatively small compared to the physical surface area of the optics, high-efficiency (but expensive) semiconductor material can be used for photovoltaic conversion, and CSP systems represent the highest-efficiency solar energy systems currently on the market [8]. The increased solar concentration creates an enormous amount of heat within the cell so an active cooling system must be incorporated into every high-concentration ratio system. Additionally, since the focusing optics require that the sun radiate at a 90° incidence angle for maximum absorption, a solar tracking system is required to track the sun across the horizon during the day. The tracking system further increases the mechanical complexity of these systems.

Despite the mechanical complexity and significant heat generated in CSP systems, semiconductor growth and processing improvements have catalyzed the wide scale implementation of CSP arrays for terrestrial energy production. Therefore, it is of great benefit to the Air Force and scientific community at large to better understand these systems at the theoretical level in order to progress this technology towards meeting the goal of military energy security and independence and decreasing dependence upon conventional non-renewable energy sources.

### 1.5 Research Focus

The purpose of this research is to improve the means for modeling and to develop a method for designing concentrated photovoltaic systems. The current dearth of

analytical research behind these optical concentrator systems has presented an exciting opportunity. Instead of relying upon empirical data to determine the optimum concentration factor, the overall goal of this research is to develop a design tool that can accurately calculate the ideal optical concentration factor based on extensive dynamic thermal modeling of the device.

The foundation of this research lies in solid state semiconductor physics. However, extensive research has also been conducted in the areas of photonics, thermal dynamics, and mathematics. Furthermore, MATLAB is used to generate the complex multi-order system models to accomplish the research goal. In particular, the following issues and questions are addressed:

1. What is the mechanism that a solar energy system uses to convert light into electricity?
2. How do the physical properties of the solar cell affect this energy conversion?
3. What are the advantages and disadvantages of concentrated solar power systems over conventional photovoltaic systems?
4. At what level do the current physical models predict the behavior of concentrated solar power systems?
5. How can the existing methods be improved to develop a new dynamic thermal model for a concentrated solar power system?
6. What benefits do the model presented provide to the existing technology?
7. How could this research be expanded in the future?
8. What are the strategic implications of renewable energy use by the military?

The increased understanding of concentrated PV systems gleaned from this research will be very beneficial to the U.S. Air Force and Department of Defense. As with most civilian technologies, further military research into terrestrial PV systems will most certainly drive the development of these technologies ahead farther and faster in the future.

# II: Theory

The theoretical analysis of a semiconductor solar cell must begin with a fundamental understanding of the solid state physics governing this device. The first goal of this analysis is to investigate the simple principle of a PN-junction under thermal equilibrium, which operationally represents a solar cell in the dark. Several important terms are presented and defined in order to lay the framework for the following analysis. The important dependency upon the excess minority carrier concentration in the device is described. Equilibrium diode currents and their associated equations are also introduced and applied to the analysis. The optical photon absorption of semiconductors is investigated introducing the photogenerated current produced across the PN-junction. Next, the nonequilbrium process of carrier generation caused by solar illumination is discussed, as applied to the simple PN-junction. Building upon this analysis, the non-uniformity of carrier generation is discussed along with the role that recombination plays in each region of the cell. Synthesizing the analysis, an expression for the excess minority carrier concentrations on each side of the junction and the resulting total current through the solar cell is derived. Finally, the fundamental solar cell parameters of open circuit voltage $V_{oc}$, short circuit current $I_{sc}$, and fill factor *ff* are defined in the context of the preceding analysis.

## 2.1 Semiconductor Physics Background

The physical principles describing semiconductor solar cells are rooted in quantum theory, the basics of which explain the concept of a semiconducting material. A semiconductor is defined by the Science Dictionary as a material with conductive

properties between those of a conductor and an insulator, and semiconductors are characterized by their atomic crystal structure [10]. Figure 3 shows a plot of several materials based on their electrical conductivities [8]. Referring to the figure, common insulators are on the left, semiconductors are in the middle, and conductors are on the right.

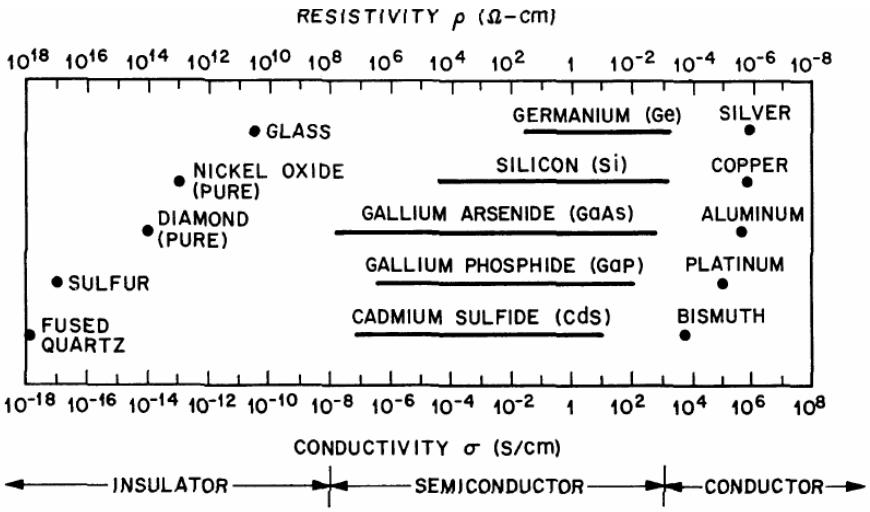


**Figure 3: Semiconductor Electrical Properties [8]**

Referring to Figure 3 another fundamental property of semiconductors is revealed- the variable electrical conductivity (and thus resistivity). Therefore, the electrical properties of semiconductors can be effectively "tuned" to generate the specific values of impedance over a given range depending on the temperature and especially the impurity doping properties of the device.

The crystal structure, or lattice, of a semiconductor is extremely important to the electrical behavior of the material. All semiconducting materials are found on the right side of the periodic table.

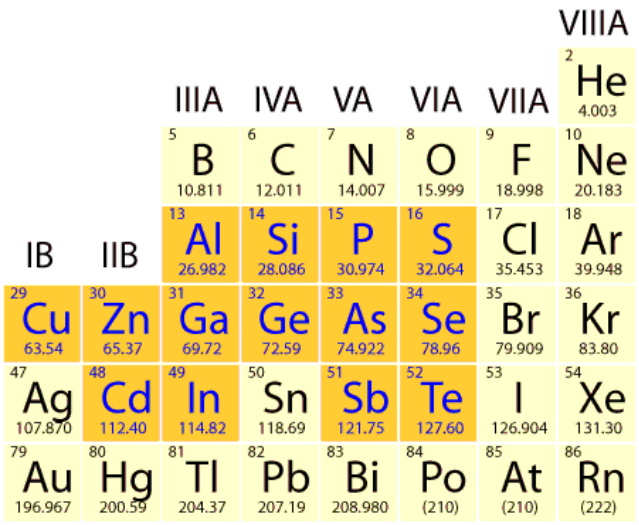


**Figure 4: Right Side of the Periodic Table Showing the Semiconducting Elements**

Most common semiconducting materials are found in groups III, IV, and V, which is very significant because the periodic group of elements is organized by outer valence electron structure, where group III elements have three valence electrons, elements in group IV have four valence electrons, and accordingly elements in group V have five valence electrons.

Semiconductors are found in both elemental (e.g. Si) and compound form (e.g. GaAs), but every semiconductor material is characterized by the properties of its crystal lattice. The covalent bonds formed within a semiconducting material determine the shape of the crystal lattice [8]. For an in depth explanation on the quantum physics governing this interaction, a Solid State Physics text book such as McKelvey's is desired, but for the sake of this analysis applied to solar cells, a cursory discussion is sufficient [10]. Most semiconductors are composed of the diamond lattice, where each atom has a covalent bond with four adjacent atoms. Compound semiconductors such as GaAs have a crystal lattice similar to the diamond lattice, but since the crystal is comprised of two

different elements, the compound semiconductor crystal lattice is referred to as the zinc blende structure as shown in Figure 5.

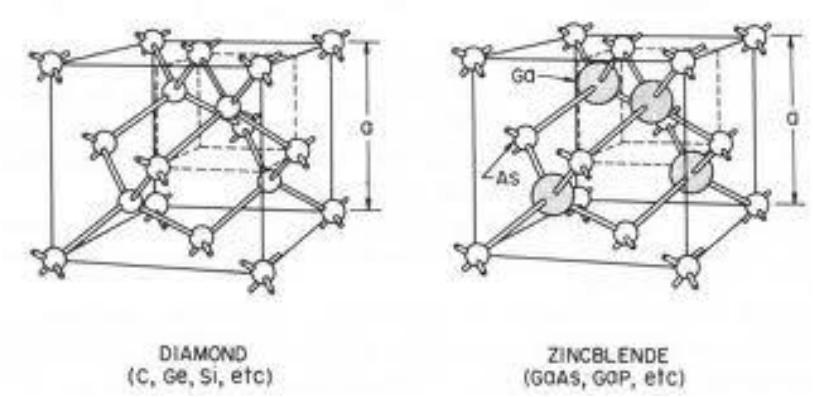


Figure 5: Diamond and Zinc Blende Lattice Structure [10]

With an appropriate understanding of the semiconductor crystal structure in hand, the electrical properties of these materials can be investigated.

## 2.2 Electrical Properties of Semiconductors

In crystalline materials such as semiconductors the electrical properties are driven by different energy levels. Electrons within a semiconductor are restricted to certain energy levels (bands) between the ground state, in which the electrons are tightly bound to the nucleus of each atom, and the free state, in which electrons are readily available for conduction [8]. The two most important energy bands within a semiconductor material are the valence band and the conduction band. The valence band $E_v$ is energetically close to the nucleus and nearly full of electrons, while the conduction band $E_c$ (next energy level up from the valence band) is only slightly filled with electrons. The amount of energy necessary to excite an electron from the valence band to the conduction band is the band gap energy $E_g$, and physically describes the energy difference between these two bands [9]. Semiconductor materials can be generally characterized as direct band gap

materials or indirect band gap materials. This characterization is based upon the nature of the energy levels within the material. Both the valence and conduction bands can be described as wave-like energy levels with varying momentum. In direct band gap materials, the band gap energy corresponds to a wave k-vector equal to zero where the minimum distance between the valence and conduction bands occurs at the same value of electron momentum, as shown in Figure 6 [10].

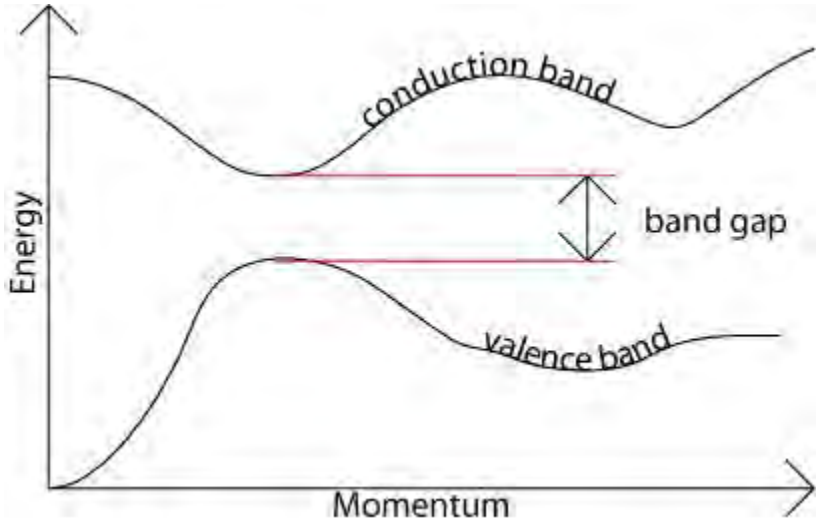


Figure 6: Direct Band Gap Semiconductor [10]

In indirect band gap materials, the k-vector does not equal zero and the minimum distance between the two bands occurs indirectly and corresponds to a difference in electron momentum between the two bands. Therefore, in an indirect band gap material shown in Figure 7, an electron cannot travel to the conduction band without a corresponding change in momentum which requires a phonon assisted transition, also known as a lattice vibration [10].

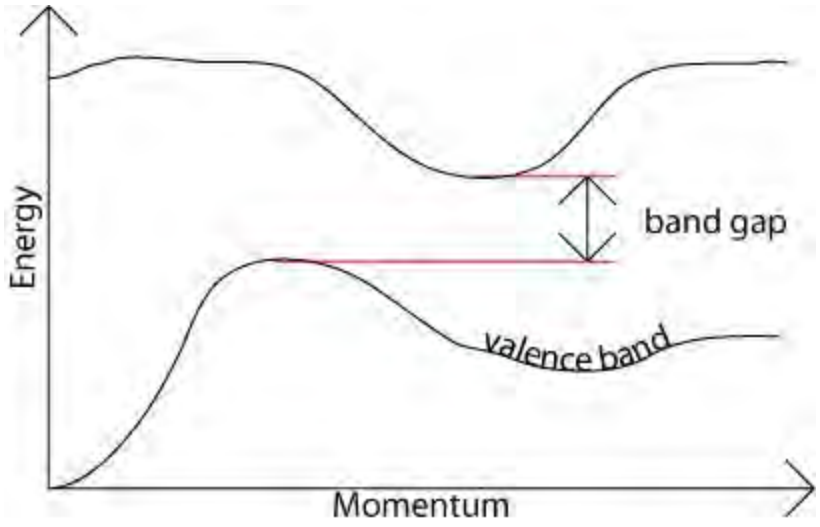


Figure 7: Indirect Band Gap Semiconductor

The intermediate energy level located between the valence and conduction bands is known as the Fermi level $E_f$, and is often used as a reference level in the analysis of semiconductors as will be shown in the following analysis. The diagram in Figure 8 shows the standard representation of an intrinsic (pure) semiconductor material, including the three energy levels discussed above.

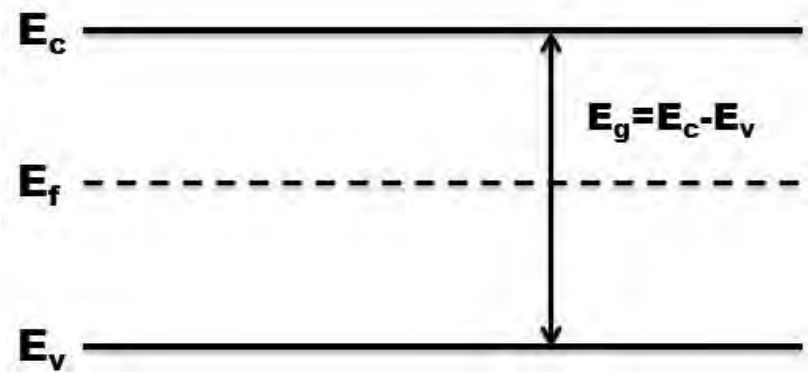


Figure 8: Equilibrium Energy Band Diagram

It is standard and accepted practice to draw the band diagram of direct and indirect band gap materials identically, since the physical significance of this difference has primarily one consequence to be discussed later in the analysis.

Classically, there are two main charge carriers within a semiconductor: electrons and holes, and each of these carriers contribute to the total electricity generated by a photovoltaic cell. A semiconductor material with an excess concentration of electrons is referred to as an *n*-type semiconductor, whereas a semiconductor with an excess concentration of holes is referred to as *p*-type. Furthermore, in extrinsic semiconductors the Fermi level, which physically describes the chemical potential of the material, is closer to the conduction band $E_c$ for *n*-type materials and closer to the valence band $E_v$ for *p*-type materials.

### 2.3 Equilibrium P-N Junction

The elemental device structure of most modern solar cells is the PN-junction, in which a semiconductor material of one conductivity type (*n* or *p*) is electrostatically joined with a semiconductor material of another type (*n* or *p*). The conductivity type of the semiconductor material is driven by the impurity doping concentration on each side of the junction, where *n*-type semiconductors have an excess of electrons and *p*-type semiconductors have an excess of holes. Extrinsic doping changes the conductivity of the semiconductor by adding charge carriers, resulting in a change in $E_f$, either raising or lowering the Fermi energy of the semiconductor relative to its intrinsic value. A PN-junction under thermal equilibrium is shown in Figure 9.

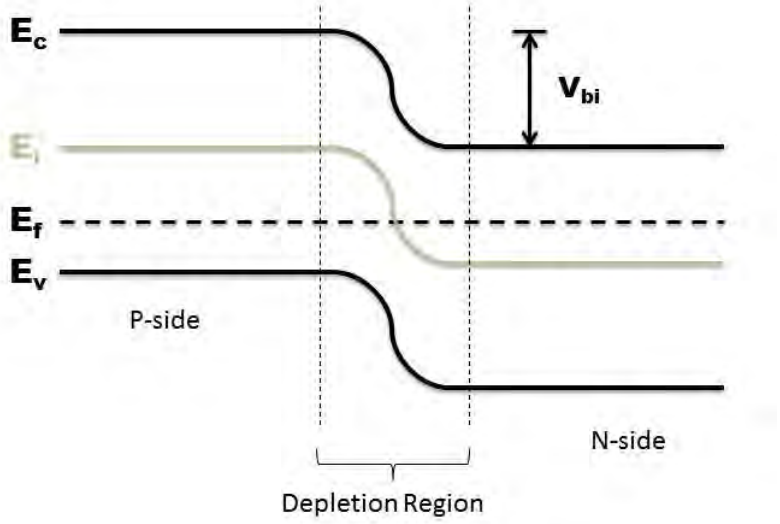


Figure 9: Equilibrium PN-junction Band Diagram

When the two sides of the PN-junction are joined together, the difference in the intrinsic Fermi energies creates a built in potential $V_{bi}$, also known as the potential barrier, across the junction but the total Fermi energy level across the entire device remains constant as shown in Figure 9. In order to conduct charge across the junction, the barrier height must be exceeded by an externally applied voltage $V_a$. Furthermore, at the junction a depletion region (also known as a space charge region) forms on either side where no carriers are present. The depletion region arises because of carrier diffusion at the junction, and the electric field over this region causes these carriers to move from one side of the depletion region to the other, provided the carriers are located within a diffusion length of the depletion region. The importance of this phenomenon cannot be understated, since it is the electric field over the depletion region that drives the main process by which light is converted into electricity. However, analytical investigation of this electric field involves a very important, fundamental assumption.

## 2.4 Poisson's Equation

The energy band diagram gives only a qualitative description of how the electric field varies over the junction, but Poisson's equation can be used to analytically describe the charge density, electric field, potential, and depletion region width of a PN-junction. Poisson's equation is written below, where φ is the potential, ρ is the charge density, $q$ is the elemental charge, $n$ and $p$ are the electron and hole densities, $N_d^+$ and $N_a^-$ are the ionized electron and hole densities, and $\varepsilon_{sc}$ is the relative permittivity of the semiconductor [14].

$$\frac{\partial^2 \varphi}{\partial x^2} = -\frac{\rho}{\varepsilon_{sc}} = -\frac{q}{\varepsilon_{sc}}(p - n + N_d^+ - N_a^-) \tag{2-1}$$

The depletion approximation allows the complex equations for the electric field, potential, and depletion region widths to be numerically solved. The depletion approximation assumes that no carriers are present in the depletion region, thus this region is fully depleted of charge carriers. The depletion approximation also assumes that the depletion region has well defined boundaries, so that the transition from the depletion region to the bulk n and p (or quasi neutral regions) regions is abrupt. The justification for use of the depletion approximation in the electrostatic analysis of a PN-junction stems from the fact that carrier concentrations change exponentially with the Fermi energy relative to the conduction band edge, and this change occurs over the depletion region as shown in Figure 9 [12]. Accordingly, the contributions of n and p over the depletion region become negligible and can be removed from the above equation, simplifying the following analysis.

$$\frac{\partial^2 \varphi}{\partial x^2} = -\frac{\rho}{\varepsilon_{sc}} = -\frac{q}{\varepsilon_{sc}}(N_d^+ - N_a^-) \tag{2-2}$$

The charge density can then be derived for four distinct regions of the device.

$$\rho(x) = 0 \qquad x_n < x < \infty \tag{2-3.1}$$

$$\rho(x) = -qN_a \quad 0 < x \leq x_n \tag{2-3.2}$$

$$\rho(x) = qN_d \quad -x_p \leq x < 0 \tag{2-3.3}$$

$$\rho(x) = 0 \quad -\infty < x < -x_p \tag{2-3.4}$$

A plot of the charge density as a function of doping and distance in a PN-junction is shown below in Figure 10.

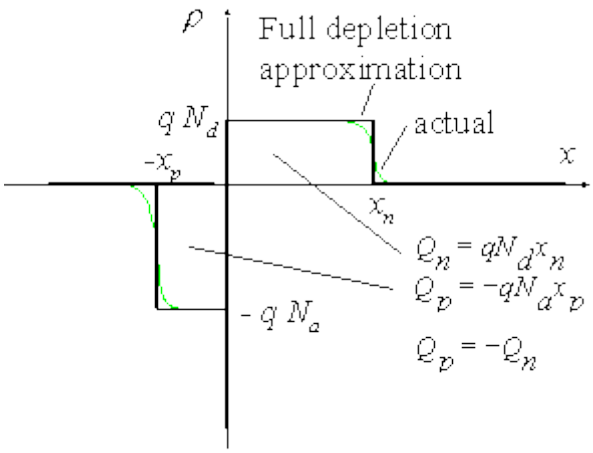


**Figure 10: PN-junction Charge Density Profile [13]**

Since charge is related to electric field $\vec{E}$ by $\frac{dE(x)}{dx} = q(N_d - N_a)$, the expressions for charge on each side of the junction can be integrated to yield the electric field over the depletion region as a function of doping and distance into the material.

$$E(x) = -\frac{qN_a(x + x_p)}{\varepsilon_{sc}} \qquad 0 < x \leq x_n \tag{2-4.1}$$

$$E(x) = \frac{qN_d(x - x_n)}{\varepsilon_{sc}} \quad -x_p \leq x < 0 \tag{2-4.2}$$

A plot of the electric field over the depletion region reveals that the greatest magnitude of the field occurs at the PN-junction as shown in Figure 11.

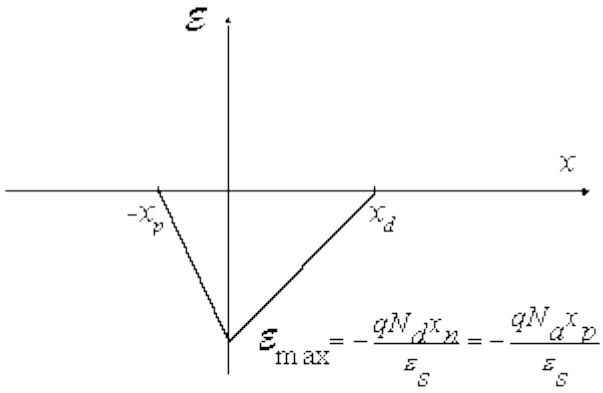


**Figure 11: Equilibrium PN-junction Electric Field [13]**

Again, the importance of this electric field over the depletion region cannot be understated. As will be shown in the following analysis, the electron drift current over this region complements the diffusion current to drive the electrical output of PN-junction solar cells. Further iterations of Poisson's equation can be solved to derive expressions for built in potential $\varphi_i$ ($V_{bi}$) and depletion region width *W* in the device, where $V_a$ is the applied voltage (zero under thermal equilibrium). The result of these calculations are shown in equations (2-5) and (2-6), but an in depth description of each step is given by Muller and Kamins [14].

$$\varphi_i - V_a = \frac{qN_d {x_n}^2}{2\varepsilon_{sc}} + \frac{qN_a {x_p}^2}{2\varepsilon_{sc}} \tag{2-5}$$

$$W = \sqrt{\frac{2\varepsilon_s}{q}\left(\frac{1}{N_a}+\frac{1}{N_d}\right)\varphi_i - V_a} \tag{2-6}$$

With expressions for the charge, electric field, potential, and depletion region width derived, the physical movement of charge carriers within an equilibrium PN-junction must be investigated.

## 2.5 Equilibrium Charge

Two equal and opposite forces dominate the movement of charges within an equilibrium PN-junction. Electron drift is the first mechanism that causes carriers to move in a PN-junction and is caused by the electric field created over the depletion region. The electric field causes carriers with the opposite charge to "drift" to each side of the junction and with respect to the band diagram shown below in Figure 12 causes electrons to roll downhill from the p-side to the n-side and holes to go uphill from the opposite direction.

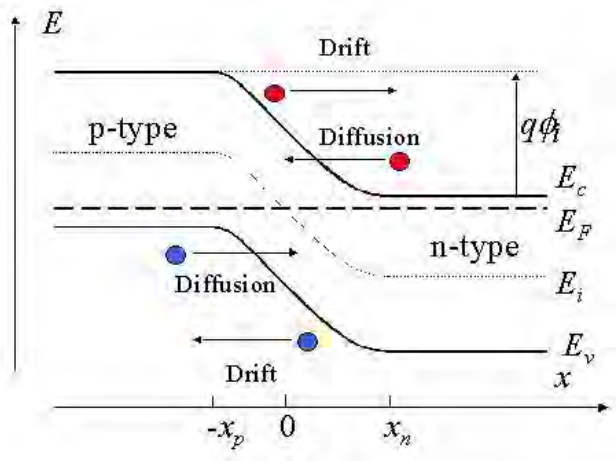


Figure 12: Charge Movement Within Equilibrium PN-junction [16]

Under thermal equilibrium, the process of electron drift is exactly balanced by the process of electron diffusion which is driven by the concentration gradient of holes and electrons at the PN-junction [11]. In much the same way that a gas diffuses into air and spreads out into a given volume, electrons and holes diffuse throughout the device once the two regions are brought into contact. Additionally, since the minority carrier concentrations on the *n* and *p*-sides will be greatest at the edge of the depletion regions, the concentration gradient causes minority carriers to diffuse away from the depletion boundaries towards the edges of the semiconductor material. The distance that the minority carriers diffuse into the semiconductor material is defined by a parameter known as the diffusion length $L_{n/p}$. As will be shown in the following analysis, once the PN-junction is disturbed from equilibrium electron diffusion will be the primary mechanism that drives the movement of charge within the bulk of the semiconductor material.

As stated in the introduction of this analysis, the equilibrium PN-junction operationally represents a solar cell in the dark- no net current flows, no external bias is applied, and the excess minority carrier concentrations are negligible. However, to make this analysis useful the condition of solar illumination must be applied, thus disturbing the simple PN-junction from equilibrium and making the analysis much more interesting.

### 2.6 Solar Illumination

Before delving into the details of the nonequilbrium PN-junction analysis it is beneficial to explain some of the important fundamental properties of solar illumination. A solar cell converts sunlight into electricity by means of the photovoltaic effect [14]. When light falls upon the surface of a semiconductor, incident photons with enough

energy break the covalent bonds within the material and free up the valence electrons for conduction. The photovoltaic effect is rooted in a concept known as the wave-particle duality of light, which states that light can simultaneously be treated as an electromagnetically radiated wave and as a particle with finite energy [8]. The latter definition lends itself well to the solid state analysis of solar cells.

The energy in solar radiation is given by $E = hv$ where $h$ is Plank's constant and $v$ is the frequency of the light. Figure 13 shows AM 1.5 solar irradiance spectrum that is used as the standard for analysis in most terrestrial solar energy systems. The frequencies of light most irradiant at the surface of the earth range from 300-750 THz. Accordingly since frequency is related to wavelength by $\lambda = \frac{c}{v}$, where $c$ is the constant speed of light ($3x10^8$ m/s), a common form for the wavelength dependent photon energy of light is $E = \frac{1.24}{\lambda}$, where λ is in μm [14]. The wavelengths of light falling on the cell above the band gap energy will vary from .4-1 μm and the associated energy range is 1.2-3.1 eV.

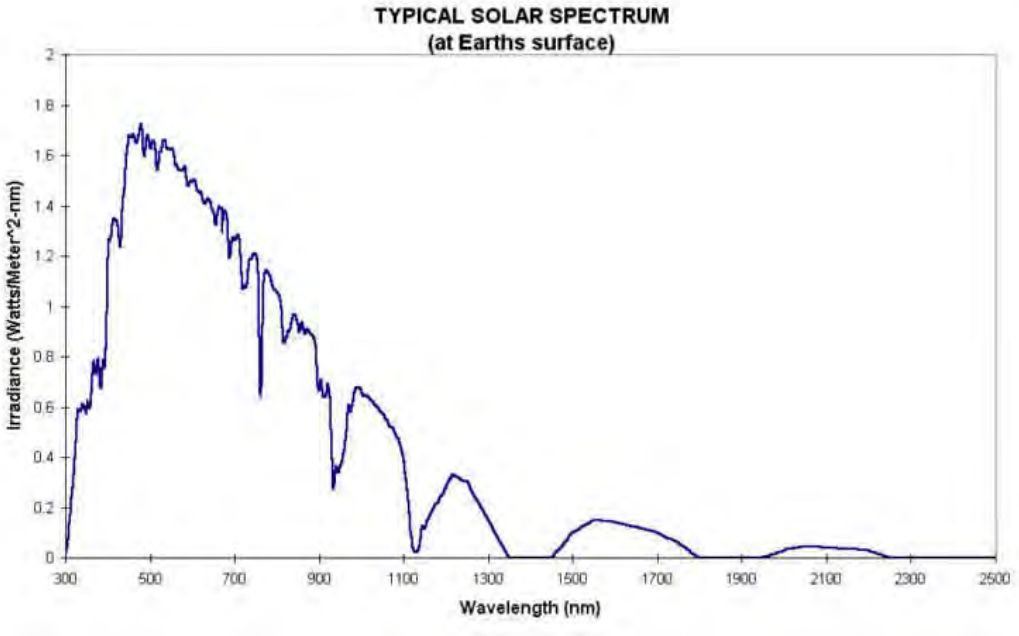


Figure 13: AM 1.5 Solar Spectrum

The bandgap energy is the amount of energy required to free an electron from its covalent bond in the semiconductor material, thus allowing it to contribute to the transfer of charge (electricity). The photon energy of the light must be at least as great as the bandgap energy of the semiconductor in order to free an electron and generate a current [15]. As incident photons with energy greater than (or equal to) the bandgap energy of the semiconductor solar cell fall onto the PN-junction, electrons are excited and electron-hole pairs are generated. However, photon energies greater than the bandgap energy also generate heat leading to thermal losses as the excited electron falls back to the edge of the conduction band. The goal of the solar cell designer is to closely match the bandgap energy of the semiconductor cell with the photon energy of incident light so that the energy production can be maximized while minimizing losses due to heat.

## 2.7 Photon Absorption and Generation

The most fundamental mechanism in the photovoltaic energy conversion process is photon absorption and the associated electron-hole pair (EHP) generation. Most solar cell models assume that every photon absorbed by the semiconductor material generates exactly one EHP [9]. Previously, it was explained that photons with energy below the semiconductor bandgap energy would not contribute to conduction and were assumed to transmit entirely through the material. However, the absorption of photons is a statistical process, and it must be stated that some photons below the band gap will contribute to the total heat generated within the solar cell, without directly contributing to the conduction of electricity across the PN-junction. Furthermore, not all photons with energy above the band gap will contribute to conduction. The quantum efficiency $\beta$ describes the percentage of photons incident on to the cell that actually contribute to charge conduction. The details of this phenomenon will be discussed later in the analysis and applied to the dynamic thermal model. Regardless, for the electrical model of the PN-junction solar cell, the former assumption that every photon absorbed generates one EHP will be used.

It is important to realize that photon absorption and electron generation are wavelength dependent properties, since different wavelengths of light carry different amounts of photon energy. Shorter wavelengths of light with higher photon energies, blue light for example, will be absorbed more readily by the material and thus do not travel as far into the PN-junction solar cell [17]. It can be assumed that for shorter wavelengths, almost all of the generation occurs near the surface of the cell. However, at longer wavelengths of light with lower photon energies, red light for example, the

photons penetrate on average entirely though the bulk of the device. Furthermore, due to the physical structure of the solar cell, all of the carrier generation will occur over the two diffusion lengths on the n and p-side and the entire depletion region, or $L_n + W + l_p$. A pictorial interpretation of this is shown in Figure 14.

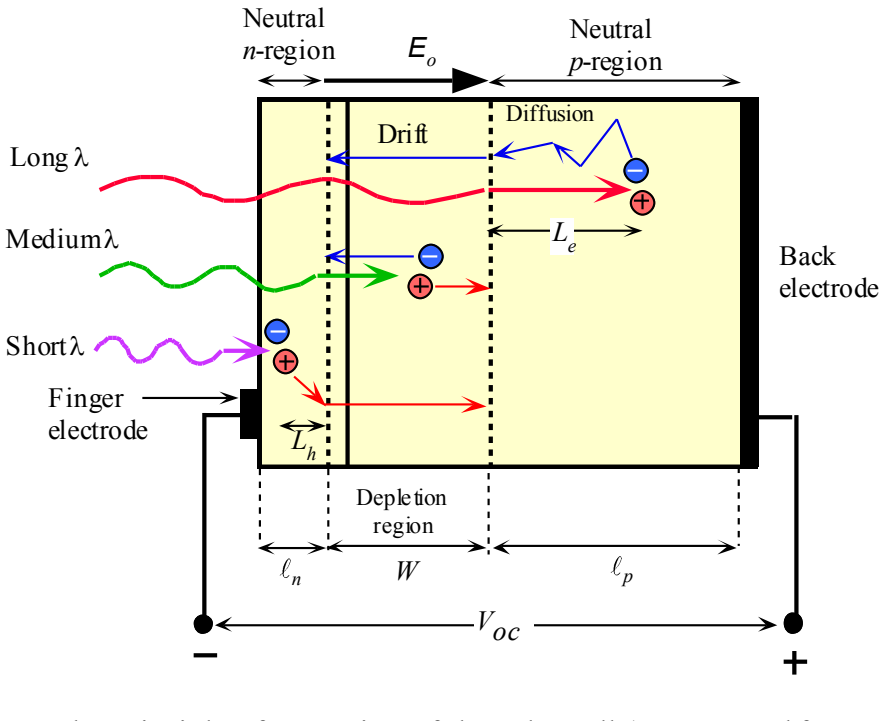


Figure 14: Photon Absorption at the PN-junction [15]

The wavelength (and thus frequency) dependent photon flux is given by $S(x,\lambda) = S_0(\lambda)e^{-\alpha x}$ where $S_0$ is the wavelength dependent number of incident photons and α is the absorption coefficient, a material dependent parameter that describes how a given material generates electrons in a device. Figure 15 shows the absorption coefficient as a function of wavelength at 300K for 7 different semiconductor materials:

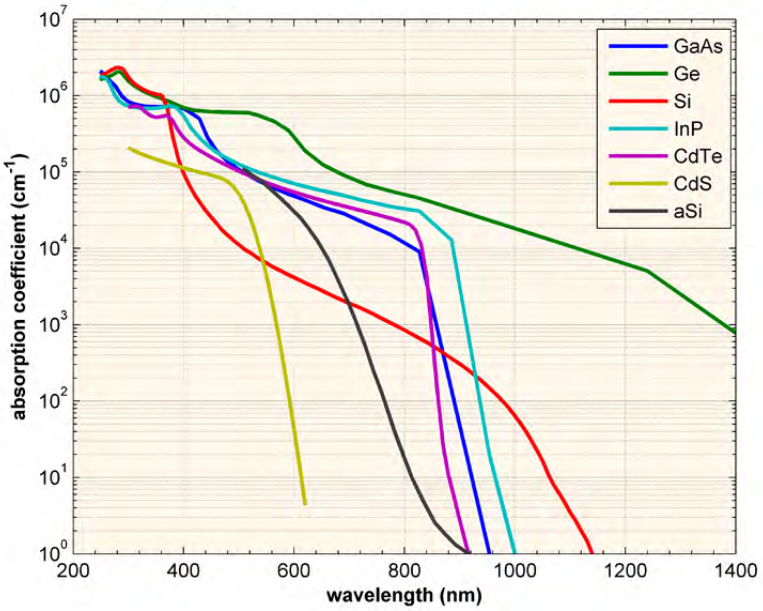


**Figure 15: Wavelength Dependent Photon Absorption for Different Semiconductor Materials [16]**

Since generation is dependent upon photon absorption, the generation rate is also a function of wavelength. However, it is useful to sum the wavelength dependent magnitude of solar irradiation in order to investigate how the generation rate varies as a function of distance into the material over the entire spectrum. Figure 16 shows a diagram of the net generation rate versus position for silicon.

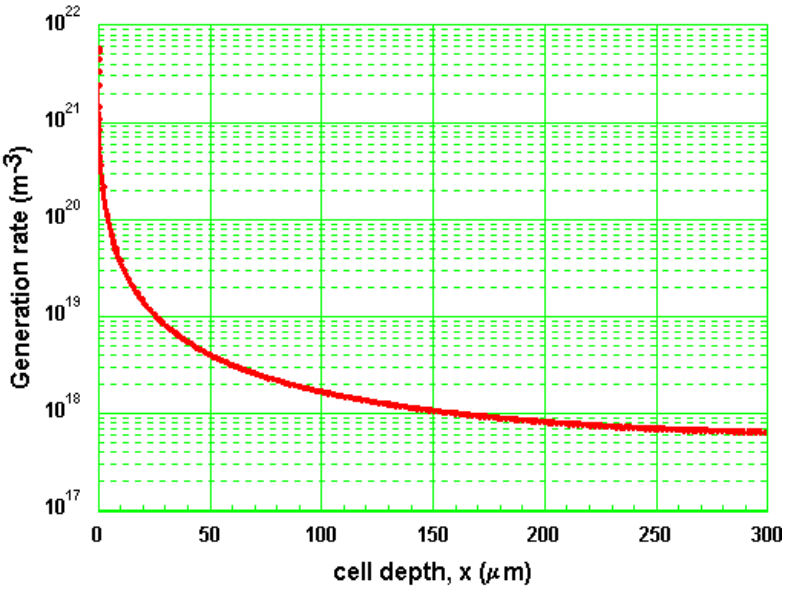


Figure 16: Generation Rate for Si

Another important optical property to discuss in the photovoltaic conversion of energy is the reflection of light off of the semiconductor surface. Often times, the reflectivity *R* is a significant detractor to the overall photon absorption so this phenomenon cannot be ignored when analyzing the generation rate within a semiconductor. The fraction of incident light that is reflected is a function of the index of refraction *n* and the extinction coefficient *k* of the material [16].

$$R = \frac{(n-1)^2 + k^2}{(n+1)^2 + k^2} \tag{2-7}$$

With photon absorption and reflection accounted for, a more realistic wavelength-dependent description of carrier generation is revealed, where *G(x, λ)* denotes position and wavelength dependent generation.

$$G(x,\lambda) = \beta(\lambda)\alpha(\lambda)S_0(\lambda)(1-R)e^{-\alpha(\lambda)x} \tag{2-8}$$

For most homojunction solar cells, the quantum efficiency β approaches unity for all wavelengths with energies greater than the bandgap energy, and for this analysis the net generation is rewritten with $G_0$ as the initial generation at the surface accounting for the reflectivity and number of incident photons.

$$G = G_0 e^{(-\alpha x)} \tag{2-9}$$

The important points to remember are that generation is greatest at the surface and decreases exponentially throughout the bulk of the cell. As was shown previously, the absorption coefficient is wavelength dependent so it follows that generation is a wavelength dependent process as well.

**2.8 Carrier Recombination**

An equally important process to carrier generation that must be discussed is carrier recombination. Recombination serves to counteract generation, in order to return the nonequilibrium cell to equilibrium, and physically describes the recombining of holes and electrons in the cell. Once an electron and hole recombine, the neutral charge is no longer available for conduction; thus, it is important to minimize carrier recombination throughout the cell in order to maximize generation and charge conduction. The process of recombination is most prevalent at impurities or defects within the crystal structure of the cell and also at the surface of the cell. Accordingly, since the process of doping intentionally introduces impurities to the crystal structure to change the electrical properties of the cell, doping consequently increases recombination in the cell [16]. Furthermore, immaculate semiconductor processing is paramount since any unintentional impurities will only enhance the carrier recombination.

There are three types of recombination in the bulk of a semiconductor solar cell: radiative recombination, Auger recombination, and Shockley-Read-Hall (SRH) recombination. Radiative recombination, also referred to as band-to-band recombination, describes the phenomenon where an electron directly recombines with a hole in the conduction band releasing a photon of light. The process of radiative recombination drives the operation of light emitting diodes (LED) and semiconductor lasers but is detrimental to the operation of a photovoltaic cell. Radiative recombination is usually neglected in the analysis of indirect bandgap semiconductors such as Silicon (Si), but this process is potentially significant for direct bandgap semiconductors such as Gallium Arsenide (GaAs).

Auger recombination is another unavoidable recombination mechanism that describes the phenomenon where an electron and hole recombine, and give the resulting excess kinetic energy to another electron in the conduction band. The excess energy given to the third carrier in the conduction band is expended in the cell as heat. Auger recombination dominates in concentrated solar cells [21].

The final recombination mechanism in semiconductor solar cells is SRH recombination. SRH recombination is due to crystal defects and is thus most important from a processing perspective, and is usually the most prevalent recombination process in a solar cell. Crystal defects, whether implanted intentionally or the product of imperfect processing techniques, introduce energy states within the bandgap energy of a PN-junction. These pseudo-energy levels known as “traps” are recombination centers in the bandgap since any electron that moves from the valence band to a trap is likely lost to recombination, especially if the trap is near the mid-band energy of the semiconductor.

SHR recombination is a two-step process where the electron moves from the valence band to the trap, and then either up to the conduction band or back to the valence band where it recombines. The process is functionally the same but reversed for holes. The rate of SHR recombination depends on the trap energy levels, where traps near the band edges are less likely to lead to recombination.

Two material parameters that are affected by recombination processes are carrier lifetime $\tau$ and diffusion length $D$. The carrier lifetime physically describes the amount of time an EHP exists in a PN-junction after generation and before recombination (or conduction). Therefore, longer carrier lifetimes are associated with less carrier recombination. The diffusion length describes the physical distance an electron or hole travels before recombining. Ideally, the diffusion length is maximized to reduce recombination. The importance of these parameters with respect to the electrical output of a PN-junction solar cell will be discussed later in the analysis. Furthermore, each of the three recombination processes will be treated simultaneously but it is beneficial to understand the three different mechanisms that an electron and hole recombine in order to minimize the detrimental effect to the overall efficiency and electrical output.

### 2.9 PN-junction Solar Cell Current

With an understanding of the equilibrium PN-junction coupled with an understanding of the role of light in photovoltaic energy conversion, it is necessary to investigate how the PN-junction changes under nonequilibrium conditions. To facilitate this analysis the ideal diode equation is applied to the solar PN-junction and the total current due to solar illumination is investigated. The value of the following model is that

the exponential generation of charge carriers is incorporated into the diode current derived from the transport and continuity equations. Most every solar cell current model currently in the literature refers to the familiar current equation that breaks the diode current $I_D$ and photogenerated current $I_{ph}$ into two separate parts, where $I_{tot}$ is the total current flowing through the cell:

$$I_{tot} = I_{ph} - I_D \tag{2-10}$$

The photogenerated current is commonly given by $I_{ph} = qG_oA(L_n + W + L_p)$, and the diode current is given by $I_d = I_0\left[e^{\frac{qV}{kT}} - 1\right]$, where $I_o$ is found using the transport and continuity equations [12].

**2.10 Solar Cell Current-Voltage Relationship**

A useful method to qualitatively examine the operation of a solar cell over the entire range of operating conditions is to plot the solar cell current versus the voltage, known as the IV curve. An example IV curve is shown in Figure 17.

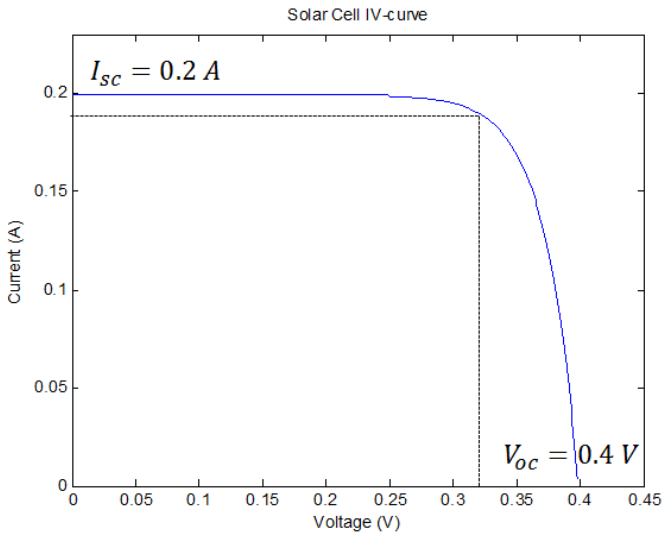


**Figure 17: Solar Cell IV Curve**

The IV characteristics of the cell clearly show the short circuit current $I_{sc}$ and the open circuit voltage $V_{oc}$, the y-intercept and x-intercept respectively, and reveal another important solar parameter known as the fill factor, denoted by *ff*. The fill factor describes the "squareness" of the IV curve since the ideal current-voltage relationship is rectangular. Therefore, it is beneficial to have the fill factor as close as possible to unity but this can never be achieved due to the exponential nature of PN-junction properties. An expression for the fill factor is defined below, where $I_m$ is the maximum operating current and $V_m$ is the maximum operating voltage.

$$ff = \frac{I_m V_m}{I_{sc} V_{oc}} \tag{2-11}$$

The maximum operating conditions $I_m$ and $V_m$ are the values where rectangular area within the IV-curve is maximized. Furthermore, the magnitude of the fill factor depends upon the device structure and material properties, but most fill factor values typically range from 0.7-0.85 [14].

## 2.11 Load Resistance

The explanation of fill factor leads into another important component of any solar power system, the load. It is necessary to connect the solar cell to a load in order to generate power. While the shape of the IV curve is independent of the load, the operating point ($I_{op}$, $V_{op}$) is determined from the load resistance. Accordingly, the operating point can be tuned to get the current and voltage as close as possible to $I_m$ and $V_m$ by matching the load resistance to the cell. Load (impedance) matching is an extremely important concept in the physical set up of solar arrays.

The operating point of the solar cell based on given load resistance $R_L$ is most easily found using a load line construction, a linear line with slope $\frac{1}{R_L}$. Figure 18 below shows a load line using a 1.68 Ω load, for the solar cell used in the previous IV curve figure.

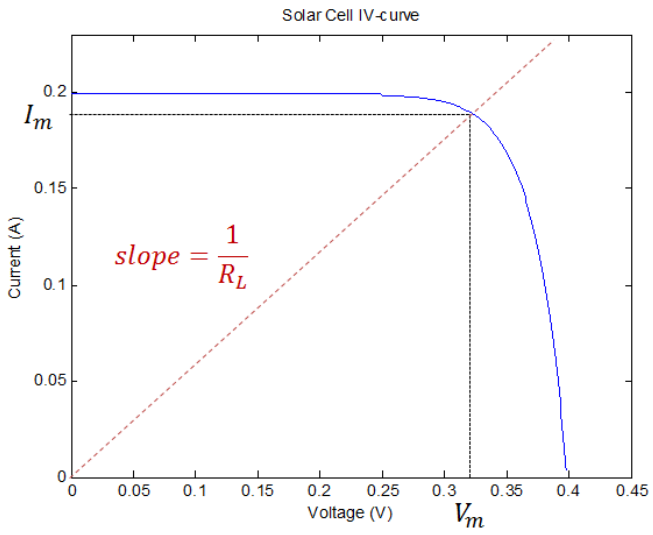


Figure 18: Load Line Plotted on IV-Curve

When the cell is connected to a load the voltage across and current through the load are equal to the voltage and current produced by the cell, but the current flows in the opposite direction. Using Ohm's law, an expression for the current through the load can be written.

$$I_{op} = -\frac{V_{op}}{R_L} \tag{2-12}$$

## 2.12 Power and Efficiency

The load serves to transform the electrical output of the cell into usable energy in the form of power. Power is the fundamental unit of electrical output for most energy systems, and most every solar array is described in terms of the total power generated. Again, this power is dependent upon the load and is optimized under load-matched conditions. The relationship between voltage, current and power is fundamental in electronics.

$$P = IV \tag{2-13}$$

The most practical measure of merit for solar cells is the electrical efficiency η, a ratio of the power incident upon the cell in the form of light $P_{in}$ to the power generated by the cell $P_{out.}$

$$\eta = \frac{P_{out}}{P_{in}} \times 100 \tag{2-14}$$

Solar cell efficiencies are generally in the range of 12% for most terrestrial non-concentrated solar cells up to 25% for highly specialized multi-junction cells designed for use in space-based or CSP systems. Several factors contribute to efficiency losses in

solar power systems, and Figure 19 summarizes the major factors decreasing this electrical efficiency.

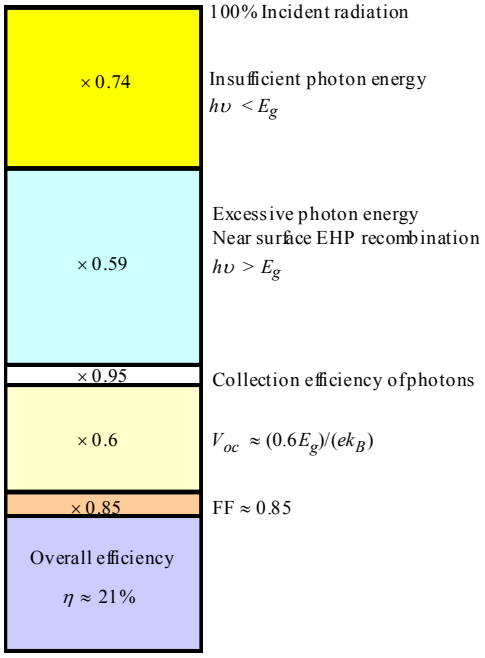


Accounting for various losses of energy in a high efficiency Si

**Figure 19: Detractors to Overall Efficiency [16]**

With an understanding of the major solar cell measures of merit, the theoretical analysis of the simple PN-junction solar cell is complete.

## 2.13 Theoretical Synopsis

To recap the analysis, the theoretical discussion of the PN-junction solar cell began with an investigation of the material properties of semiconductors and an explanation of their characteristic crystal structure. A short explanation of the atomic bonding within a semiconductor material was discussed and the periodic table was referenced showing groups III-V, the most important groups to the semiconductor industry.

Following the atomic level discussion, an introduction to the quantum physics governing the electrical properties of semiconductors was presented. Several

fundamental properties were examined including the conduction band, valence band, Fermi level, and band gap energy. The difference between direct and indirect semiconductors was also explained.

Next, the PN-junction was introduced opening the door to further discussion of semiconductor devices in the context of solar cells, and Poisson's equation was used to solve for the electric field, potential, and depletion region width in the junction. The charge distribution within the device was analyzed to prepare for nonequilibrium effects caused by solar irradiance.

The important concepts of solar radiation in the AM 1.5 spectrum were discussed to lay the framework for the solar illumination analysis. Following, the fundamental concept of carrier generation caused by solar irradiance was presented, along with the opposite process of carrier recombination.

Finally, the solar cell photocurrent was investigated to create the total current-voltage relationship. The concepts of short circuit current, open circuit voltage, and fill factor were defined as applied to the characteristic solar cell IV-curve. To wrap up the theoretical analysis, power output and efficiency were described and defined as the two most important measures of merit for practical solar power systems.

**2.14 Literature Review**

Since the goal of this research is to improve the modeling of solar concentrator systems, it is necessary to investigate the models currently used in industry to design these systems.

Following the familiar equation used in the initial analysis, most models serve to derive both components of the current using the assumption of *constant* generation

throughout the device. However, this is an oversimplification of the total current since the diode current and photocurrent are inherently dependent upon each other [14]. Furthermore, uniform generation throughout the device is not a practical assumption, especially given the wavelength dependent absorption coefficients for most semiconductor materials compared to their common manufactured thicknesses for use as solar cells.

Simplified assumptions regarding excess carrier generation ultimately lead to a simplified expression for diode current throughout the device. A common method used to determine the diode current in a PN-junction solar cell is to solve for the minority carrier distributions using the Shockley method for a short-base *n*-side and long base *p*-side junction without incident light, shown graphically in Figure 20 [12].

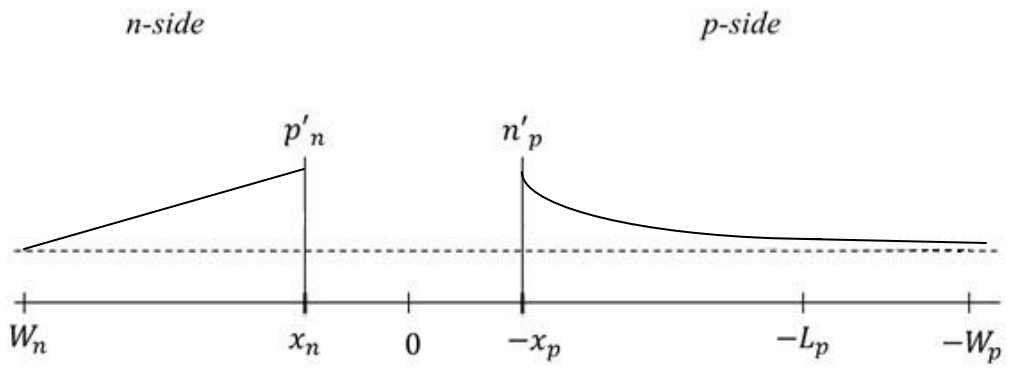


**Figure 20: Short Base (n-side) Long Base (p-side) PN-junction [12]**

Referring to Figure 20 $W_n$ is the surface of the device (facing the sun), $x_n$ is the depletion region boundary on the n-side, $p'_n$ is the excess concentration of holes on the n-side, $n'_p$ is the excess concentration of electrons on the p-side, $-x_p$ is the depletion region boundary on the p-side, $-L_p$ is the diffusion length for electrons on the p-side, and $-W_p$ is the physical boundary of the device. The model shown in Figure 20 proves valid for a

simple semiconductor PN-junctions under forward bias but is an oversimplification when used for solving the diode current in a solar cell. The condition of photon absorption in solar cells introduces excess carriers that are generated in the bulk of the surface (*n*-side) layer. Therefore, the excess carrier concentration will be greater than zero near the surface of the device and at a maximum in the bulk of the surface layer. The resulting expression for diode current, derived in the next chapter, is much more complete when surface recombination and bulk photon absorption is included.

Other solar cell models attempt to approximate excess carrier concentration in a PN-junction solar cell as a negative exponential throughout the device as shown in Figure 21 [19].

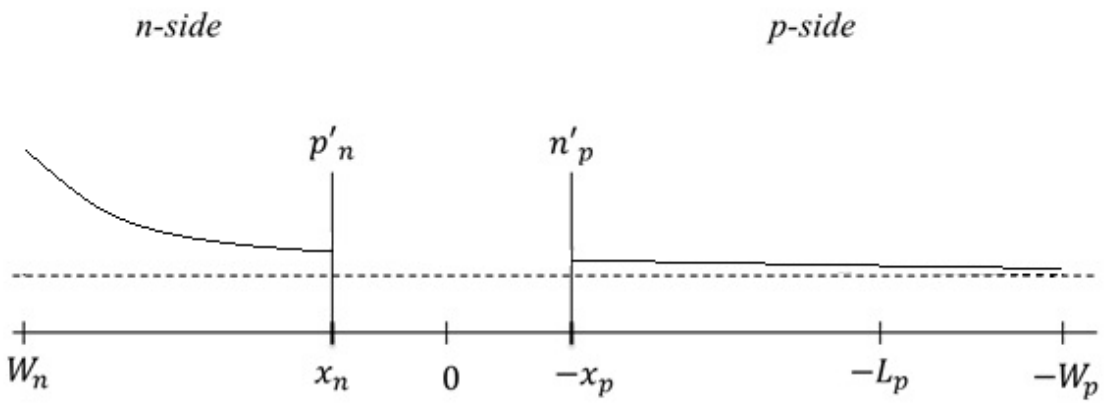


**Figure 21: Exponential Model for Excess Carrier Concentration**

The exponential model for excess carrier concnetration is also an oversimplification. As shown previously in Figure 16, photon generation can be modeled by an exponential, but the phenonomenon of surface recombination (discussed in Section 2.8) serves to reduce the excess carrier concentration at the surface of the device to nearly zero. Incorporating the effect of surface recombination dramatically changes the

resulting equation for current through the device, as will be shown in the following analysis.

Another issue with modeling excess carrier concentration through the device as an exponential arises when the diffusion length approaches the photon penetration depth. This anomaly can be seen in the equation for the photogenerated current using this method, where $J_\alpha$ is the photocurrent, $q$ is the elemental charge, $A$ is the surface area of the cell, $\alpha$ is the inverse of penetration depth, $G_o$ is the generation rate at the surface, and $L_n$ is the diffusion length for holes on the n-side (absorption layer) [19].

$$J_\alpha = qA\left(\frac{\alpha G_o}{\frac{1}{{L_n}^2} - \alpha^2}\right) \tag{2-15}$$

A mathematical singularity arises when ${L_n}^2 = \frac{1}{\alpha^2}$ since the denominator of equation (2-15) becomes zero, and the photogenerated current becomes infinite. The exponential model for excess carrier concentration was initially used as the foundation for this research until this singularity was discovered. Other authors have alluded to the relationship between diffusion length and photon penetration depth, but it was confirmed that when mulitple suns are used to illuminate the cell, the rise in cell temperature causes these two quantities to approach equivalence [22]. An important consequence of this discovery is the realization that the electrical model plays an important role in determing steady state temperature, since the wrong model can lead to drastically extreme values for photogenerated current under certain conditions leading to an overestimation of the heat generated in the device. Therefore, further investigation into the excess carrier

concentration disrtibution throughout the device was necessary, and a new model was develped to serve as the foundation for this research.

Several simple solar cell models are presented in the academic literature. While some of these models oversimplify significant phenomena, there are benefits to using such simple models in large-scale applications. In situations where the power generated by an array of non-concentrated terrestrial solar cells exceeds the kilowatt range, absolute efficiency becomes less important than raw power generated. Accordingly, when analyzing these systems, elemental dependence upon carrier concentrations under different illumination conditions such as clouds or fog proves rather insignificant to the broad scale application.

Furthermore, the solar cell models generated using the solid state physics approach cannot accurately predict the operation of non-crystalline solar cells. Amorphous and organic cells that are populating the research as third generation cells are not easily predicted using detailed numerical analysis. Analysis of these cells is generally done empirically as current-voltage curves can be drawn for any photovoltaic cell. Also, the physical transition from low-level injection to high-level injection as a function of concentration ratio is not well defined, but it has been demonstrated that very high levels of concentration move the solar cell device to high-injection, where the presented model proves invalid [17] [18].

The most significant difference between the solar cell models currently in the literature and the model presented in this research is that the model presented here quantifies the change in voltage and current of the cell as a function of the dynamic thermal effects of the cell under illumination. Under concentration the cell will heat up

and the device parameters will change, but there are few models that adequately investigate this phenomenon. No other solar cell model currently in the literature has solved the transport and continuity equations, simultaneously with the heat equations, to investigate the effect of temperature on the important device parameters under low-level injection. Consequently, this research is beneficial to the Air Force engineering community especially given that the Air Force has begun installation of several CSP systems across the country.

This analysis serves to forgo the simplification used often in photovoltaic current solutions by solving the transport and continuity equations using a gamma distribution approximation for the excess minority carrier concentration throughout the device. As will be seen, the total current derived using this approach is not nearly as aesthetic or straightforward to derive, but as with most complex mathematical models, more accurately predicts the physical operation of the device. In addition, a more accurate current model lends to a better foundation for the final dynamic thermal model of the CSP system, as will be shown in the following analysis.

## III: Gamma Distribution Excess Minority Carrier Concentration Model

Accounting for exponentially decaying generation using a gamma distribution approximation for excess minority carrier concentration proves complex. However, as will be shown, the resulting differential equations can be analytically solved to yield a more accurate representation of the minority carrier concentrations and resulting current through the device.

### 3.1 Ideal Diode Analysis

The ideal diode equation can be used to solve for the total current through the PN-junction solar cell. Solar illumination introduces the nonequilibrium processes of carrier generation and recombination. While no external bias is applied to the junction, generation of carriers within the electric field of the depletion region effectively causes the PN-junction to be forward biased. To model the electrical characteristics of a photovoltaic cell, a solution to the time dependent diffusion equation for a single PN-junction is investigated. The device is analyzed using the ideal diode equation. The goal of this analysis is to characterize the solar cell by investigating the photogenerated diode currents within the PN-junction under solar illumination. Since ideal diode currents are driven by minority carriers, the excess minority carrier concentration on each side of the PN-junction must be determined.

### 3.2 Solar Cell PN-junction

Generally, a simple semiconductor solar cell can be modeled as a PN-junction with a relatively large depletion region and an asymmetric base length for the n and p-side. An n-type semiconductor material is commonly used for the thinner absorption

layer, while p-type material usually comprises the thicker base region because the diffusion length for electrons is much longer than the diffusion length for holes. Thus, creating a thicker p-type region allows for maximum diffusion of minority carriers [21].

Following the analysis demonstrated by Muller and Kamins, the n-side of the junction (facing the sun) is treated as a short base case since the diffusion length is over the entire depth of the junction [14]. Accordingly, the p-side is treated as a long base case since the diffusion length is much less than the width of the cell [11]. Figure 22 shows a diagram of the cell under solar illumination.

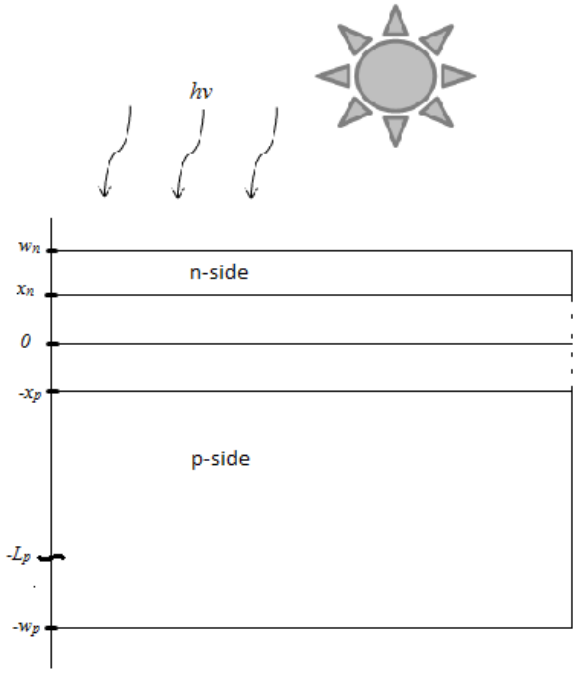


**Figure 22: PN-junction Solar Cell Under Illumination**

It is important to note that, given the condition of low level injection, the diode current in a PN-junction is driven by the excess minority carrier concentration (holes on

the n-side and electrons on the p-side). Thus in order to solve for the current across the PN-junction we need to know the minority carrier concentration on each side.

### 3.3 Minority Carrier Concentrations

The excess minority carrier concentration on the n-side of an ideal short base diode under forward bias can be approximated by a linear function, provided there is no carrier generation present. However, the phenomenon of carrier photo-generation coupled with surface recombination lends the excess minority carrier concentration distribution to approximate a gamma function (with shape parameter equal to two).

The gamma distribution PDF is shown below [25]:

$$y(x) = \frac{1}{b^a \Gamma(a)} x^{a-1} e^{-\frac{x}{b}} \tag{3-1}$$

In the gamma PDF equation, $a$ is the shape parameter, $b$ is the scale parameter, and $\Gamma$ is the gamma function term. The interesting conclusion- that the gamma distribution can be used to model excess minority carrier concentration in a solar cell- is a unique and novel contribution of this research. Several other excess minority carrier concentration distributions were investigated, but no other distribution was able to account for both the high surface recombination rate and penetration of photons into the bulk of the device, and it has been demonstrated that surface recombination is a particularly important phenomenon in PN-junction silicon solar cells [25]. The gamma distribution makes sense physically because the excess minority carrier concentration at the surface of the device (where recombination is high) is negligible, while the concentration peaks at a depth into the device where generation is high and

recombination is low, before exponentially decaying throughout the rest of the device. A plot of the gamma distribution reveals the physical approximation of the excess minority carrier concentration on the n-side of a solar cell.

On the *p*-side of the junction the excess minority carrier concentration can be approximated by an exponential function [11]. A plot of the excess minority carriers for a forward-biased solar cell with photo-generation present is shown in Figure 23, where $p'_n$ and $n'_p$ are the excess holes and electrons respectively, $x_n$ and $x_p$ are the depletion region edges, and $W_n$ and $W_p$ are the boundaries of the device.

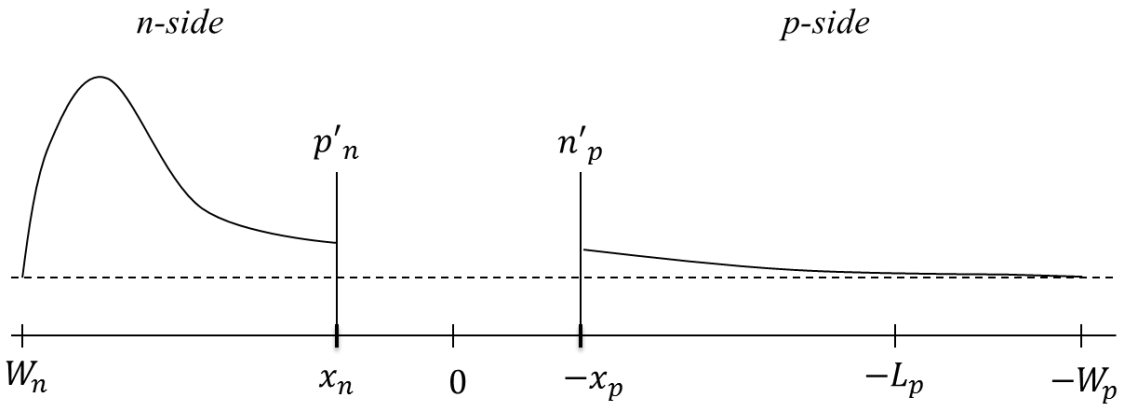


**Figure 23: Minority Carrier Concentration Across the PN-junction**

The plot of the minority carrier concentrations shown in Figure 23 assumes bulk recombination and incorporates exponential EHP generation, with the sun facing the n-side. The magnitude of the generation $G_0$ caused by illumination exponentially decreases through the one-dimensional depth of the material (*x*-direction into the PN-junction), as modeled by $G_0 e^{-\alpha x}$ and shown in Figure 24.

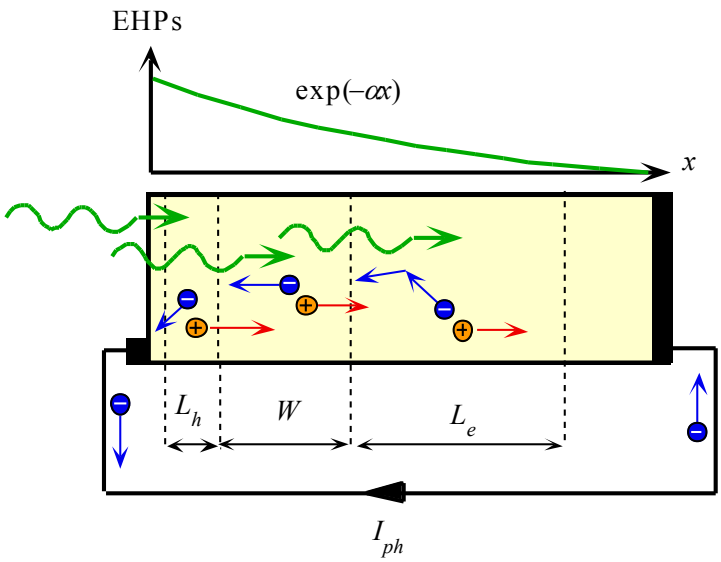


Photogenerated carriers within the volume $L_h + W + L_e$ give rise to a photocurrent $I_{ph}$. The variation in the photogenerated EHP concentration with distance is also shown where $\alpha$ is the

**Figure 24: Exponential Generation [14]**

Furthermore, while no external applied voltage is present on the n-side, the solar illumination that generates carriers causes the PN-junction to be forward biased. To investigate the flow of charge through the device under forward bias given the excess minority carrier concentrations shown above, it is necessary to solve the fundamental charge transport equations on both sides of the PN-junction solar cell.

### 3.4 Continuity Equation

The differential continuity equation for the minority carrier concentration on the n-side of the solar cell is shown below [18]:

$$\frac{\partial p'n}{\partial t} = D_p \frac{\partial^2 (p'n)}{\partial x^2} - \mu_p E(x) \frac{\partial (p'n)}{\partial x} + g'(x) - \frac{p'n}{\tau_{po}} \tag{3-2}$$

In the above equation *p'n* is the minority carrier concentration on the n-side (holes), $D_p$ is the diffusion coefficient for holes, $\mu_p$ is the mobility for holes, *E(x)* is the electric field in the region, *g'(x)* is the generation term for holes in the n-side, $\tau_{po}$ is the carrier lifetime, and *x* represents the one-dimensional distance into the region.

An analogous equation can be written for minority carriers on the p-side *n'p* [20].

$$\frac{\partial n'p}{\partial t} = D_n \frac{\partial^2 (n'p)}{\partial x^2} + \mu_n E(x) \frac{\partial (n'p)}{\partial x} + g'(x) - \frac{n'p}{\tau_{no}} \tag{3-3}$$

Since we are solving for the steady state condition of the solar cell, the time based derivative of minority carrier concentration on the n-side $\frac{\partial p'n}{\partial t}$ is set equal to zero. Furthermore, using the depletion approximation, the electric field in both the n and p-side (outside the depletion region) can be set to zero.

$$0 = D_p \frac{\partial^2 (p'n)}{\partial x^2} + g'(x) - \frac{p'n}{\tau_{po}} \tag{3-4.1}$$

$$0 = D_n \frac{\partial^2 (n'p)}{\partial x^2} + g'(x) + \frac{n'p}{\tau_{no}} \tag{3-4.2}$$

Dividing this equation by the diffusion coefficient $D_p$ yields a familiar form for a second order homogenous differential equation, where the diffusion length $L_p$ is given as $\sqrt{D_p \tau_{po}}$.

$$0 = \frac{\partial^2(p'n)}{\partial x^2} + \frac{g'(x)}{D_p} - \frac{p'n}{{L_p}^2} \tag{3-5.1}$$

$$0 = \frac{\partial^2(n'p)}{\partial x^2} + \frac{g'(x)}{D_n} - \frac{n'p}{{L_n}^2} \tag{3-5.2}$$

As shown above in Figure 24 the generation term *g'(x)* can be modeled as a decaying exponential term. The generation rate will be highest at the surface of the solar cell, since the light intensity will be greatest at the surface, and the rate depends upon the absorption coefficient α (material property) and the initial generation rate $G_0$ (function of how strong the light is at the surface). Accordingly, the generation rate can be modeled by the term $g'(x) = G_0 e^{-\alpha x}$ [9].

The resulting differential equation must be solved for *p'n* to determine the minority carrier concentration on the n-side assuming high surface recombination and exponentially decaying generation [13]. It is important to realize that the entire solution for the minority carrier concentration on the n-side will be the sum of the particular and homogenous solutions.

### 3.5 Particular Solution to the Transport Equation

To determine a particular solution for *p'n* in the second order differential equation shown above, a conjecture must be made to the form of the solution. It follows, from the form of the second order differential equation shown in (3-5.1), that a gamma PDF $p'_n = \frac{\beta\delta^2}{\Gamma(2)} x e^{-\delta x}$ is a reasonable guess to the form of the particular solution for carrier

concentration, where δ and β are "dummy" variables used to satisfy the mathematical operations. This assumption can be verified by plugging the particular solution into the second order differential equation shown in equation (3-6). The assumption is valid as long as the particular solution yields a non-trivial solution for the minority carrier concentration.

The first step in determining the validity of the gamma distribution assumption is to solve equation (3-6) using the minority carrier concentration *p'n* on the n-side. The easiest way to solve this equation is to first solve for each of the three parts of equation (3-6).

$$0 = D_p \frac{\partial^2(p'n)}{\partial x^2} + g'(x) - \frac{p'n}{\tau_{po}} \tag{3-6}$$

$$D_p \frac{\partial^2(p'n)}{\partial x^2} = D_p \frac{\beta\delta^2(x\delta^2 e^{-\delta x} - 2\delta e^{-\delta x})}{\Gamma(2)} \tag{3-7}$$

$$g'(x) = G_0 e^{-\alpha x} \tag{3-8}$$

$$-\frac{p'n}{\tau_{po}} = -\frac{\beta\delta^2 x e^{-\delta x}}{\Gamma(2)\tau_{po}} \tag{3-9}$$

$$D_p \frac{\beta\delta^2(x\delta^2 e^{-\delta x} - 2\delta e^{-\delta x})}{\Gamma(2)} + G_0 e^{-\alpha x} - \frac{\beta\delta^2 x e^{-\delta x}}{\Gamma(2)\tau_{po}} = 0 \tag{3-10}$$

The exponential terms can be eliminated by dividing into each term of equation (3-10). When the three parts of equation (3-6) are plugged in using the particular solution as shown in equation (3-10), a non-trivial solution for β (independent of x) is found when $\delta = \alpha$.

$$D_p \frac{\beta\delta^2(x\delta^2 - 2\delta)}{\Gamma(2)} + G_0 - \frac{\beta\delta^2 x}{\Gamma(2)\tau_{po}} = 0 \tag{3-11}$$

$$D_p \frac{\beta\delta^2(-2\delta)}{\Gamma(2)} + G_0 = 0 \tag{3-12}$$

$$\beta = \frac{G_o \Gamma(2)}{2D_p \alpha^3} \tag{3-13}$$

The initial generation rate at the surface of the solar cell is given by $G_0$ while the total generation is given by β and is independent of distance into the material from the original particular solution to the differential equation (3-5.1).

### 3.6 Recombination Coefficient Solution

In the second order differential equation for excess minority carrier concentration shown above, carrier recombination is modeled by the term $-\frac{c_o}{\tau_{po}}$, where $c_o = \frac{\beta\delta^2 x e^{-\delta x}}{\Gamma(2)}$ is the recombination coefficient. Furthermore, a gamma distribution function was used to solve the differential equation since it was shown that surface recombination is high in PN-junction solar cells. To fundamentally understand the mechanism of recombination in terms of the carrier transport equation it is necessary to solve for the recombination coefficient $c_o$ in terms of photon penetration.

As will be shown, the recombination coefficient invokes a correction factor that allows a solution to the differential equation using the gamma function to be found. Without the recombination coefficient figured into the transport equation, the model fails

to satisfy the continuity equation, and the gamma function "guess" does not solve the second order differential equation. Therefore, this recombination coefficient is imminently important in the rest of the model.

To investigate the recombination term, the second order differential terms dependent upon x must be separated.

$$D_p \frac{\beta\delta^2(x\delta^2)}{\Gamma(2)} - \frac{\beta\delta^2 x}{\Gamma(2)\tau_{po}} = 0 \tag{3-14}$$

$$D_p\delta^2 - \frac{c_o}{\tau_{po}} = 0 \tag{3-15}$$

With $\delta = \alpha$, an expression for the recombination coefficient $c_o$ in terms of photon penetration and diffusion length can be found.

$$D_p\alpha^2 - \frac{c_o}{\tau_{po}} = 0 \tag{3-16}$$

$$D_p\alpha^2 = \frac{c_o}{\tau_{po}} \tag{3-17}$$

$$L_p{}^2\alpha^2 = c_o \tag{3-18}$$

The recombination coefficient shown above allows the transport equations to be solved using the gamma distribution.

### 3.7 Homogenous Solution the Transport Equation

With a particular solution to the original second order differential equation, the homogenous solution must be determined to derive an expression for the entire minority carrier concentration on the n-side. The form for homogenous solution for this differential equation is shown in equation (3-19) [13].

$$p'n = Ae^{\frac{-(x-x_n)}{L_p}} + Be^{\frac{(x-x_n)}{L_p}} \tag{3-19}$$

To determine the homogenous solution for the minority carrier concentration on the n-side it is necessary to use boundary conditions to solve for the coefficients *A* and *B* [11].

The first boundary condition used to solve for the homogenous solution to this second order differential equation is derived from the ideal diode law, which states that no excess minority carrier concentration is present at the outside edge $x_n + x_p$ (surface) of the material. Therefore, the minority carrier concentration at the surface is given by equation (3-20).

$$p'n(x_n + W_n) = \frac{G_o\Gamma(2)}{2D_p\alpha^3} = Ae^{\frac{-(x_b)}{L_p}} + Be^{\frac{(x_b)}{L_p}} + \frac{G_o\Gamma(2)}{2D_p\alpha^3} \tag{3-20}$$

$$0 = Ae^{\frac{-(x_b)}{L_p}} + Be^{\frac{(x_b)}{L_p}} \tag{3-21}$$

$$A = -Be^{\frac{(2x_b)}{L_p}} \tag{3-22}$$

With a solution to one of the coefficients, a second boundary condition must now be applied. The second boundary condition relies on the depletion approximation and states that no recombination is present at the edge of the depletion region $x_n$. Furthermore, at the depletion region boundary the excess minority carrier concentration due to generation will be $\frac{G_o\Gamma(2)}{2D_p\alpha^3}$ per the particular solution, but the total excess minority carrier concentration will be dependent upon the magnitude of the forward bias $V_a$ caused

by the generation of carriers under illumination. The result of the second boundary condition yields another solution for the coefficients.

$$p'n(x_n) = p_{no}\left(e^{\frac{qV_a}{kT}} - 1\right) + \frac{G_o\Gamma(2)}{2D_p\alpha^3} = A + B + \frac{G_o\Gamma(2)}{2D_p\alpha^3} \tag{3-23}$$

$$p_{no}\left(e^{\frac{qV_a}{kT}} - 1\right) = A + B \tag{3-24}$$

Using the coefficient equation derived using the first boundary condition, a solution for both coefficients can be found.

$$A = -Be^{\frac{2x_b}{L_p}} \tag{3-25}$$

$$p_{no}\left(e^{\frac{qV_a}{kT}} - 1\right) = -Be^{\frac{2x_b}{L_p}} + B \tag{3-26}$$

$$B = \frac{p_{no}(e^{\frac{qV_a}{kT}} - 1)}{(1 - e^{\frac{(2x_b)}{L_p}})} \tag{3-27}$$

$$A = -\frac{p_{no}(e^{\frac{qV_a}{kT}} - 1)e^{\frac{2x_b}{L_p}}}{(1 - e^{\frac{(2x_b)}{L_p}})} \tag{3-28}$$

### 3.8 Total Excess Minority Carrier Concentration on the n-side

Once the two coefficients have been found, a final expression for the excess minority carrier concentration on the *n*-side as a function of one dimensional distance *x* into the material and intensity of light (quantified by $V_a$) can be defined.

$$p'n(x) = Ae^{\frac{-(x-x_n)}{L_p}} + Be^{\frac{(x-x_n)}{L_p}} + \frac{G_o\Gamma(2)}{2D_p\alpha^3} \tag{3-29}$$

$$p'n(x) = \left[ -\frac{p_{no}(e^{\frac{qV_a}{kT}} - 1)e^{\frac{2x_b}{L_p}}}{(1 - e^{\frac{(2x_b)}{L_p}})} \right] e^{\frac{-(x-x_n)}{L_p}} + \left[ \frac{p_{no}(e^{\frac{qV_a}{kT}} - 1)}{(1 - e^{\frac{(2x_b)}{L_p}})} \right] e^{\frac{(x-x_n)}{L_p}} + \frac{G_0 x e^{(x-x_n)\alpha}}{2D_p \alpha^3} \tag{3-30}$$

With an expression of the excess minority carrier concentration on the n-side, an expression for the current density ($A/m^2$) in terms of hole current $J_p$ through the n-side of the junction under forward bias caused by illumination can be written.

$$J_p = qD_p \frac{dp'n}{dx} \tag{3-31}$$

$$J_p = -qD_p \left[ \left[ \frac{p_{no}(e^{\frac{qV_a}{kT}} - 1)e^{\frac{2x_b}{L_p}}}{(1 - e^{\frac{(2x_b)}{L_p}})} \right] \frac{e^{\frac{-(x-x_n)}{L_p}}}{L_p} + \left[ \frac{p_{no}(e^{\frac{qV_a}{kT}} - 1)}{(1 - e^{\frac{(2x_b)}{L_p}})} \right] \frac{e^{\frac{(x-x_n)}{Lp}}}{L_p} + \frac{G_0 \left( \frac{1}{\alpha} + (x_b - x_n) \right)}{2D_p} \right] \tag{3-32}$$

### 3.9 Boundary Conditions for the p-side

Now that the current on the n-side of the solar cell PN-junction has been characterized, the current on the p-side must be investigated. As stated earlier, the continuity equation says that the total current throughout the device must be constant under steady state conditions, therefore it is most convenient to solve for the two currents at the depletion region boundaries $x_n$ and $-x_p$ and sum these components to get the total current through the device.

### 3.10 Constant p-side Generation Assumption

To analyze the p-side of the solar cell PN junction another important assumption is made: the generation rate is constant throughout the *p*-side of the junction. This assumption proves practical given the physical construction of most semiconductor solar cells, where two differently doped layers are brought into contact one on top of the other as shown in Figure 22. Accordingly, given the one-dimensionality of the device, most all of the carrier generation will occur on the top layer of the PN junction, and for the sake of this analysis the carrier generation throughout the bottom p-side layer is assumed to be γ.

### 3.11 Continuity Equation for p-side

The homogenous equation for the p-side excess minority carrier concentration is rewritten below:

$$0 = \frac{\partial^2(n'p)}{\partial x^2} + \frac{g'(x)}{D_n} - \frac{n'p}{{L_n}^2} \tag{3-33}$$

The assumption that generation is constant lends a much more aesthetic solution to this second order differential equation. Furthermore, the solution for the excess minority carrier concentration on the long base p-side (assuming bulk recombination and constant generation) has been well documented in the literature and an adequate analysis was followed by Honsberg. The resulting general solution to this differential equation is shown below in equation (3-34), where γ denotes the excess minority carrier concentration due to constant generation $\frac{G_0 {L_n}^2}{D_n}$.

$$n'p = Ae^{\frac{(x+x_p)}{L_n}} + Be^{\frac{-(x+x_p)}{L_n}} + \gamma \tag{3-34}$$

It is important to note that $\frac{G_o\Gamma(2)}{2D_p\alpha^3}$ is the carrier concentration due to generation at the depletion region edge of the n-side of the junction, and the assumption follows that the carrier concentration due to generation is also constant throughout the depletion region and the p-side of the junction. However, the form of the carrier concentration term due to generation will change slightly. Following a similar boundary condition analysis done for the n-side of the PN-junction, a solution for the minority carrier concentration as a function of *x* on the *p*-side is derived. The first step is to solve for the minority carrier concentration at the depletion region boundary $-x_p$ to solve for the homogenous coefficients *A* and *B* using boundary conditions similar to ones used in the analysis on the n-side of the junction. The first boundary condition says that the excess minority carrier concentration will be greatest at the depletion region edge $-x_p$ once an external voltage (due to illumination) is applied. Again, γ refers to the constant generation throughout the bulk of the p-side.

$$n'p(-x_p) = n_{po}\left(e^{\frac{qV_a}{kT}} - 1\right) + \gamma = Ae^{\frac{-(x_b)}{L_p}} + Be^{\frac{(x_b)}{L_p}} + \gamma \tag{3-35}$$

$$n_{po}\left(e^{\frac{qV_a}{kT}} - 1\right) = Ae^{\frac{-(x_b)}{L_p}} + Be^{\frac{(x_b)}{L_p}} \tag{3-36}$$

$$A = -Be^{\frac{(2x_b)}{L_p}} + n_{po}\left(e^{\frac{qV_a}{kT}} - 1\right)e^{\frac{(x_b)}{L_p}} \tag{3-37}$$

The second boundary condition says the minority carrier concentration on the p-side at the far end of the junction past the diffusion length (deep into the device) will be near the equilibrium concentration $n_{po}$ along with the constant generation term γ.

$$n'p(L_p) = \gamma = Ae^{\frac{-(x_b)}{L_p}} + Be^{\frac{(x_b)}{Lp}} + \gamma \tag{3-38}$$

$$0 = Ae^{\frac{-(x_b)}{Lp}} + Be^{\frac{(x_b)}{Lp}} \tag{3-39}$$

$$0 = \left[-Be^{\frac{(2x_b)}{L_p}} + n_{po}\left(e^{\frac{qV_a}{kT}} - 1\right)e^{\frac{(x_b)}{L_n}}\right]e^{\frac{-(x_b)}{Lp}} + Be^{\frac{(x_b)}{L_p}} \tag{3-40}$$

$$-n_{po}\left(e^{\frac{qV_a}{kT}} - 1\right) = -Be^{\frac{(x_b)}{Lp}} + Be^{\frac{(x_b)}{Lp}} \tag{3-41}$$

$$B = B \equiv 0 \tag{3-42}$$

Therefore *B* must equal zero to satisfy the homogenous solution to the second order differential equation shown above, which follows from the long base case coefficient analysis demonstrated by Muller in Kamins. Furthermore, upon inspection this seems appropriate because of the exponential term $Be^{\frac{-(x+x_p)}{L_p}}$ following the coefficient *B* in the homogenous equation. At first glance, this term appears to be a negative exponential but reviewing the reference dimensions used in Figure 22 reveals that indeed this term will be a positive exponential once the proper negative x-position into the material is used in the solution. It follows that there should not be any positive exponential terms in the excess minority carrier concentration equation at the far end of the diffusion length into the p-side material.

### 3.12 Excess Minority Carrier Concentration on p-side

With both coefficients considered, the resulting solution to the second order differential equation can be found.

$$n'p = Ae^{\frac{(x+x_p)}{L_p}} + Be^{\frac{-(x+x_p)}{L_p}} + \frac{G_0{L_n}^2}{D_n} \tag{3-43}$$

$$n'p = \left[n_{po}\left(e^{\frac{qV_a}{kT}} - 1\right)e^{\frac{(x_b)}{Lp}}\right]e^{\frac{(x+x_p)}{L_p}} + \frac{G_0{L_n}^2}{D_n} \tag{3-44}$$

It has been shown that the excess minority carrier concentration on the p-side is also a function of the magnitude of forward bias $V_a$ caused by solar illumination. With an expression of the excess minority carrier concentration on the p-side assuming constant generation, an expression for the current density through the p-side of the junction under forward bias caused by illumination can be written.

$$J_n = qD_n \frac{dn'p}{dx} \tag{3-45}$$

$$J_n = qD_n \left[ \left[ n_{po} \left( e^{\frac{qV_a}{kT}} - 1 \right) e^{\frac{(x_b)}{L_p}} \right] \frac{1}{L_p} e^{\frac{(x+x_p)}{L_p}} \right] \tag{3-46}$$

### 3.13 Total Diode Current

The diode current can be effectively described by the sum of the currents on both the n and p-side of the junction, at each depletion region boundary. A complete expression for the current density through the device that accounts for the contribution of both the *p*-side and *n*-side is written below.

$$J_{tot} = J_p(x_n) + J_n(-x_p) = qD_p \frac{dp'n(x_n)}{dx} + qD_n \frac{dn'p(-x_p)}{dx} \tag{3-47}$$

$$J_{tot} = -qD_p \left[ \left[ \frac{p_{no}(e^{\frac{qV_a}{kT}} - 1)e^{\frac{2x_b}{L_p}}}{(1 - e^{\frac{(2x_b)}{L_p}})} \right] \frac{1}{L_p} + \left[ \frac{p_{no}(e^{\frac{qV_a}{kT}} - 1)}{(1 - e^{\frac{(2x_b)}{L_p}})} \right] \frac{1}{L_p} + \frac{G_0(\frac{1}{\alpha} + (x_b - x_n))}{2D_p} \right] + qD_n \left[ \left[ n_{po} \left( e^{\frac{qV_a}{kT}} - 1 \right) e^{\frac{(x_b)}{L_n}} \right] \frac{1}{L_n} \right] \tag{3-48}$$

The total current $I_{tot}$ ($A$) can be found by multiplying the current density by the effective area of the solar cell. Again, it is important to note that these equations hold as long as the device operates under the condition of low level injection. The dependence of the minority carrier concentration, and thus total current, on $V_a$ uncovers an ostensibly contradictory relationship (since we determined that $p'_n$ was not a function of applied voltage), but upon further investigation an interesting phenomenon is explained. With no external applied voltage the diode current is just a function of this generation. If no generation were present, as is the case with the classical PN-junction under thermal equilibrium, then no net diode current would be present without an applied voltage. This is the case of the solar cell in the dark.

# IV: Thermal Analysis

As the solar cell collects light from the sun, especially under concentration, the physical temperature of the cell rises. Explained earlier in the analysis, the process of EHP generation creates excess energy that is expended through the cell as heat. Solving for the current in the cell allows for further investigation into the dynamic thermal properties of the semiconductor solar cell under concentration. The current produced through the PN-junction solar cell produces heat generated due to solar illumination and the associated electrical output. Fundamentally, from an electronics perspective, a PN-junction solar cell behaves as a resistor to current flow when an external circuit is connected. As the photocurrent through the junction increases (illumination and carrier generation increases) more power, and thus heat, is created throughout the device. The total current provides the framework from which heat through the solar cell can be investigated.

## 4.1 Temperature Effects

With an expression for total current through the PN-junction solar cell, accounting for exponentially decaying generation throughout the device, thermal properties of the cell under illumination can be investigated. Before jumping into the analytical modeling of heat generated throughout the solar cell, it is beneficial to understand which properties of the PN-junction solar cell depend upon temperature in order to predict what properties are going to change once the temperature of the cell increases.

Temperature is proportional to thermal energy within a semiconductor [8]. As temperature increases, the kinetic energy of atoms within the crystal lattice of a

semiconductor is increased. As the temperature of a semiconductor increases, the band gap energy $E_g$ decreases [14]. Accordingly, several other semiconductor material parameters are affected by changes in temperature as well. As the band gap energy of a semiconductor decreases, the amount of photons available for conduction increases since lower energy photons can then be readily absorbed under increased temperature. It follows that lower energies are required to break the covalent bonds within the material as the temperature increases.

An increase in cell temperature causes the conductivity σ to increase while decreasing the carrier mobility μ, which increases the flow of current within a PN-junction solar cell. However, this increase in charge flow is dominated by a larger decrease in voltage across the junction, effectively decreasing the overall efficiency of the cell as the temperature increases. Investigating the fundamental device equations quantitatively describes exactly how the PN-junction changes with temperature. The fundamental investigation of the benefit caused by increased photon generation due to solar concentration opposed by the loss of efficiency due to rising cell temperature is the crux of this analysis. As will be shown, adequate cooling of concentrated solar power systems is vital to their successful operation.

### 4.2 Diode Current-Temperature Relationship

The simplified diode current $I_d$ (derived assuming constant generation) contains an observable temperature dependence [12].

$$I_d = I_0 \left[ e^{\frac{qV_a}{kT}} - 1 \right] \tag{4-1}$$

As the temperature of the cell increases, the magnitude of the diode current appears to decrease exponentially. Further investigation of the equation for diode current reveals that the reverse saturation current $I_0$ is also dependent upon temperature. The equation for the reverse saturation current in a semiconductor is given by (4-2), where $q$ is the elemental charge, $A$ is the area of the cell, $D_p$ and $D_n$ are the diffusivities of holes and electrons (a function of doping), $L_p$ and $L_n$ are the diffusion lengths holes and electrons, $N_A$ and $N_D$ are the doping levels, and $n_i$ is the intrinsic carrier concentration (material property) [12].

$$I_o = qAn_i{}^2\left[\frac{D_n}{L_nN_D} + \frac{D_p}{L_pN_A}\right] \tag{4-2}$$

The most interesting parameter, for the sake of thermal analysis, in the equation for reverse saturation current (4-2) is the intrinsic carrier concentration $n_i$, and it is assumed in the equation that $n_i{}^2 >> N_D$ and $N_A$. The intrinsic carrier concentration dependence on temperature is given in equation (4-3), where $m^*_{e/h}$ are the effective electron and hole masses, and $B$ is a temperature independent material property [20].

$$n_i{}^2 = 4\left(\frac{2\pi kT}{h^2}\right)^3 (m_e^* m_h^*)^{3/2} e^{\frac{-Eg}{kT}} = BT^3 e^{\frac{-Eg}{kT}} \tag{4-3}$$

The equation for $n_i$ is quite complex, but it is evident that the intrinsic carrier concentration is dependent upon both the band gap energy of the semiconductor and the temperature. The expanded equation for intrinsic carrier concentration can be plugged into the saturation current equation to reveal the important temperature dependence on both the saturation and diode currents.

$$I_o = qABT^3 e^{\frac{-Eg}{kT}}\left[\frac{D_n}{L_n N_D} + \frac{D_p}{L_p N_A}\right] \tag{4-4}$$

$$I_d = \left[qABT^3 e^{\frac{-Eg}{kT}}\left[\frac{D_n}{L_n N_D} + \frac{D_p}{L_p N_A}\right]\right]\left[e^{\frac{eV}{kT}} - 1\right] \tag{4-5}$$

Therefore, by inspection, it can be seen that as the temperature increases the diode current increases as well, validating the previous assertion. However, the increase in diode current with temperature fails to portray the complete interaction; the junction voltage must now be investigated.

### 4.3 Voltage-Temperature Relationship

The electric field across the junction is also affected by temperature. As the temperature increases, the electric field experiences a significant reduction in magnitude. Furthermore, as the temperature increases the depletion region width *W* decreases as well. The equation for open circuit voltage shows an obvious temperature dependence, where $I_{ph}$ is the simplified current due to illumination and $I_o$ is the reverse saturation current [14].

$$V_{oc} = kTln(\frac{I_{ph}}{I_o}) \tag{4-6}$$

A relationship showing the quantitative open circuit voltage difference for two different temperatures assuming constant bandgap energy can also be derived [15].

$$V_{oc2} = V_{oc1}\left(\frac{T_2}{T_1}\right) + E_g(1 - \frac{T_2}{T_1}) \tag{4-7}$$

It is not immediately apparent, but when realistic values for temperature, open circuit voltage, and band gap energy are input into the equation above the resulting open circuit voltage decreases as temperature rises. Using an initial open circuit voltage of 0.6

V, an increase in temperature of 40 °C from 300 K yields a 12% decrease in the resulting open circuit voltage for Silicon. The magnitude of this open circuit voltage decrease far overshadows the small increase in diode current effectively decreasing the electrical output of the cell. A qualitative assertion, based on the preceding analysis of the ideal PN-junction solar cell, reveals that a necessary goal of the solar cell designer should be to reduce the cell operating temperature to increase both output and efficiency.

### 4.4 Heat Generated

There are three components contributing to the heat generated in a PN-junction solar cell. The first component of heat is due to the photons of light below the band gap energy that do not have enough energy to excite electrons up to the conduction band. These low energy photons, while not contributing to conduction, still contribute to thermal losses in the cell due to the atom interactions within the lattice, causing weak atomic vibrations that generate heat.

It is important to note that heat generated (and dissipated) can be expressed in terms of power, and for the sake of the thermal analysis "power" will refer to heat. To derive the expression for power generated due to photon absorption $P_\tau$ below the bandgap the reflection coefficient $R$ must be mentioned, a material property that describes quantitatively how many photons reflect off the surface of a semiconductor material (see Section 2.7). The power generated depends on the reflection coefficient since any photons that reflect off the solar cell surface will not contribute significantly to heat generated.

While most commercial solar cells use some form of anti-reflection (AR) coating, the assumption is made that the test cell is free of any AR material, simplifying the modeling of reflection in the simulation. Furthermore, all of the effective wavelengths below the bandgap must be accounted for and given the diagram of the AM 1.5 solar spectrum, it is clear that there will be a large range of wavelengths emitted by the sun below the band gap of most semiconductors. To include all effective wavelengths, the wavelength dependent generation must be integrated from the lowest wavelength up to the band gap energy. The resulting expression for the power generated by photons below the band gap is shown in equation (4-8), where $A$ is the effective area of the cell, $G(\lambda)$ is the wavelength dependent generation, and $R$ is the reflection coefficient.

$$P_T = A(1-R)\int_0^{\lambda_{Eg}} G(\lambda)d\lambda \tag{4-8}$$

The second component of heat in the PN-junction solar cell is generated by the flow of current through the cell given by $P_I$. Incident photons with energy at the bandgap excite electrons from the valence band up to the conduction band. This conduction produces the current derived in the preceding analysis. The power generated due to illumination is assumed to be constant across the area of the cell. This seems a valid assumption given that the physical area of the concentrated solar cell is small so that the focusing optics can be configured to uniformly illuminate the surface [21]. Non-uniform illumination in concentrated solar cells was investigated by Luque et al., and it was concluded that these effects are incredibly complex to model [22].

Given uniform illumination and EHP generation, the component of heat due to illumination is given by the power dissipated across the junction, where $I_{tot}$ is the total solar cell current, and $R_{cell}$ is the equivalent resistance of the solar cell.

$$P_I = I_{tot} R_{cell}^2 \tag{4-9}$$

The final component of heat generated in the PN-junction solar cell is caused by incident photons with energy greater than the bandgap energy of the semiconductor. As explained earlier, these photons excite electrons past the conduction band, forcing electrons to relax back to the edge of the conduction band. The excess amount of energy above the band gap that a photon has is expended through the cell as power given by $P_p$.

The derivation of the expression for power generated by photons above the band gap is very similar to the expression for power generated due to photons below the band gap. However, the quantum efficiency β must now be included since not all of the photons above the band gap will be absorbed by the semiconductor. Furthermore, to account for all of the effective wavelengths of solar radiation, the wavelength dependent generation term must be integrated over all wavelengths above the associate band gap energy wavelength. The resulting term for the power generated due to photons above the band gap is shown in equation (4-10), where β is the quantum efficiency, $hv$ is the energy of light, $E_g$ is the band gap energy and $G(\lambda)$ is again the wavelength dependent generation.

$$P_p = A\beta \int_{\lambda_{Eg}}^{\infty} (hv - E_g) G(\lambda) d\lambda \tag{4-10}$$

The three terms contributing to the power generated in a PN-junction solar cell derived above provides an adequate description for the entire heat generated in the cell.

### 4.5 Heat Dissipated

The total temperature in the PN-junction solar cell is not only a function of power generated in the cell but also a function of the power dissipated throughout the cell. There are two primary mechanisms that serve to dissipate power in a concentrated solar cell. Black body emission $P_{bb}$ is the first mechanism that removes heat from a cell, since any object that absorbs electromagnetic radiation also dissipates a fraction of that radiation as heat. In reality, a true black body radiator cannot exist, but the law still applies for solar cells since a significant amount of radiation incident upon the surface of the cell is absorbed. Since this phenomenon is an emission versus absorption, the effective change in temperature of the cell is negative.

The black body heat phenomenon was first described by Max Planck, and an eloquent solution is given for the heat generated by a black body emitter as a function of temperature, surface area, and the Stefan-Boltzmann constant σ [23].

$$P_{BB} = A\sigma T^4 \tag{4-11}$$

The second mechanism that serves to remove power from the solar cell is due to convection currents created by active cooling systems. These active cooling systems are standard in most concentrated solar cells and are found in a variety of forms using various coolant liquids such as air, water, and other fluids [21]. For the sake of this analysis, air is the primary coolant and thus the heat convection is a function of the air temperature and flow rate across the surface of the cell. In thermodynamic analysis of the solar cell, the physical surface of the cell is treated as a simple 2-dimensional plate. The power transferred $P_c$ from the plate to the laminar air stream provided by the active

cooling system is given by the expression below, where $h_{plate}$ is the heat transfer coefficient of the semiconductor material, A is the effective area of the cell, $T_{cell}$ is the temperature of the cell, and $T_\infty$ is the temperature of the laminar cooling stream [23].

$$P_C = h_{plate} A(T_{cell} - T_\infty) \tag{4-12}$$

Another heat dissipation method used in most solar cells is the physical heat sink. Using a heat sink to dissipate heat from the cell is an effective measure in cells with large surface areas. However, heat sinks must also dissipate heat through some form of a convective cooling mechanism. It is also important to note that heat transfer by means of conduction was neglected from the total heat equation, since the physical width of the device is so small.

**4.6 Total Heat**

With the five main components of heat in the solar cell accounted, an expression for the total power can be written.

$$P_T = P_\tau + P_I + P_p - (P_c + P_{BB}) \tag{4-13}$$

When the total power approaches zero a steady state temperature point is reached where the power generated in the cell is exactly balanced by the power dissipated. Initially, the power generated in the cell will be greater than the power dissipated but as time continues and all other factors are controlled the two mechanisms removing heat from the cell will eventually settle the solar cell temperature to a new equilibrium temperature. It is important to realize that the convective cooling system serves to keeps the solar cell from heating up to thermal runaway, a disastrous positive feedback condition for semiconductors in which the cell heats up to failure [25]. As long as the

cooling system is sufficient, the convective cooling apparatus will remove a significant portion of the heat generated and a steady state temperature will be reached.

The goal of the dynamic thermal model is to iteratively solve the continuity equation for different temperatures, accounting for the five components of power discussed above, in order to analytically determine exactly when this steady state temperature point is realized.

The value of this analysis is that it can quantitatively determine optimum concentration factors for a CSP system under low levels of concentration because the only factor that will fundamentally change the dynamic nature of the model (and effective increase in temperature) is the magnitude of solar irradiation. Since it was determined previously in the analysis that the photocurrent generated in a cell linearly increases with solar irradiation, while the effective increase in temperature serves to decrease the electrical output, an optimum balance between concentration ratio and temperature must be achieved assuming that the active cooling mechanism remains constant. The thermal model will be run for varying levels of concentration to investigate the associated increases in cell temperature. Obviously, lower concentration factors will lead to lower cell temperatures, and the thermal model will reach steady state more quickly than high concentration ratios. Additionally, at lower concentrations the magnitude of the current will be lower than for higher concentrations. The goal is to determine where the two quantities are optimized.

Another important consideration stems from a fundamental assumption used in this analysis, the assumption of low-level injection operating conditions. Under low level injection, changes in majority carrier concentrations are insignificant relative to the

minority carrier concentrations. Thus, the majority carrier concentrations on either side of the PN-junction remain constant. However, the process of concentration serves to drastically change the carrier concentrations, as shown previously, and at very high levels of concentration low level injection no longer applies. Once the device changes from low to high level injection conditions, most all of the preceding analytical derivations for carrier concentrations, depletion region width, and electric field prove invalid. Therefore, this thermal model only deals with low level injection and accordingly only low concentration ratios.

### 4.7 Thermal Model

The fundamental idea behind the dynamic thermal model of a PN-junction solar cell under concentration is relatively straightforward. The continuity equation derived a PN-junction under illumination is solved under steady state conditions for one concentration and a range of different temperatures, and the total power is calculated at each temperature. The temperature at which the power generated equals the power dissipated (thus total power equals zero) is the steady state temperature. Furthermore, IV-curves are plotted for each temperature to easily investigate how the fill factor and open circuit voltage change with temperature. The MATLAB code generated for the thermal model is included in Appendix A.

# V: Test Cell Characterization

In order to verify the accuracy of the theoretical thermal model presented in this work, it is necessary to conduct laboratory tests on a solar cell under maximally controlled conditions. Furthermore, to ensure that the conducted tests are as thorough as possible, it is necessary to completely characterize the material properties of the test cell to input into the computer model, so that the two results (physical and theoretical) can be simultaneously compared and analyzed.

The solar cell used throughout testing is a simple commercially available polysilicon cell. A chronological and reproducible series of steps was performed to characterize the material properties of the test cell. First, the junction capacitance of the cell was measured to investigate the impurity doping concentrations of the PN-junction. Next, the effective cell thickness was measured using a scanning electron microscope (SEM). Following the SEM measurement, the reverse saturation current was calculated from $N_a$ and $N_d$ to investigate the n-side and p-side thicknesses individually. The final characterization step was performed using the doping concentrations, thicknesses, and resistivities to determine the internal resistance of the cell. It is important to realize that all characterization tests of the cell were performed with the cell in the dark to maximize the control of the tests and to evaluate the test cell as an ideal diode.

## 5.1 Phase Shift Method to Determine Junction Capacitance

A very clever method for determining doping levels indirectly through variations in junction capacitance was demonstrated by Hinken, Milsted, et al. A diagram of the test set-up is shown in Figure 25.

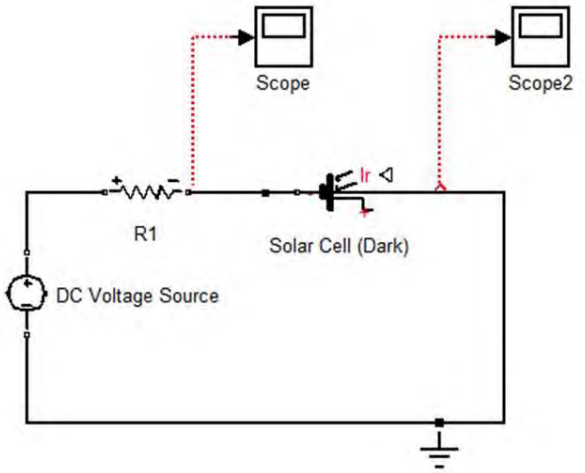


Figure 25: CV Measurement Test Diagram

The capacitance-voltage (CV) measurement technique is an established technique to accurately determine impurity concentrations in PN-junction solar cells [27], and this test is primarily conducted in the time domain by measuring the transient decay of a voltage step through the cell. However, this method proved difficult in the lab because of the relatively large capacitance of the voltage source used to generate the applied voltage. Therefore, this CV-test was performed in the frequency domain to measure the phase shift of the output sinusoidal waveform from the solar cell (in the dark) as compared to the input.

A PN-junction under thermal equilibrium can be modeled as a capacitor, where the parallel plates are the quasi-neutral n and p-sides of the device separated physically by the width of the depletion region. The theory behind the test is grounded in the fact that the capacitance of a PN-junction diode changes with applied voltage, since the width of the depletion region also changes with applied voltage as discussed in Chapter III.

$$C' = \sqrt{\frac{q\epsilon_s NaNd}{2(\frac{kT}{q}\ln\left(\frac{NaNd}{ni^2}\right) + V_R)(Na + Nd)}} \quad (5\text{-}1)$$

In the equation above $V_R$ is the applied voltage across the cell. The capacitance of the cell under zero applied voltage can be directly measured with a multimeter. But, the capacitance of the cell under applied bias must be measured indirectly with the frequency domain CV-test. Using the set up shown in Figure 25, the phase shift of the output waveform compared to the input was measured for the solar cell with an applied voltage of approximately -6.6 V. A diagram of the output waveform from the oscilloscope is shown in Figure 26.

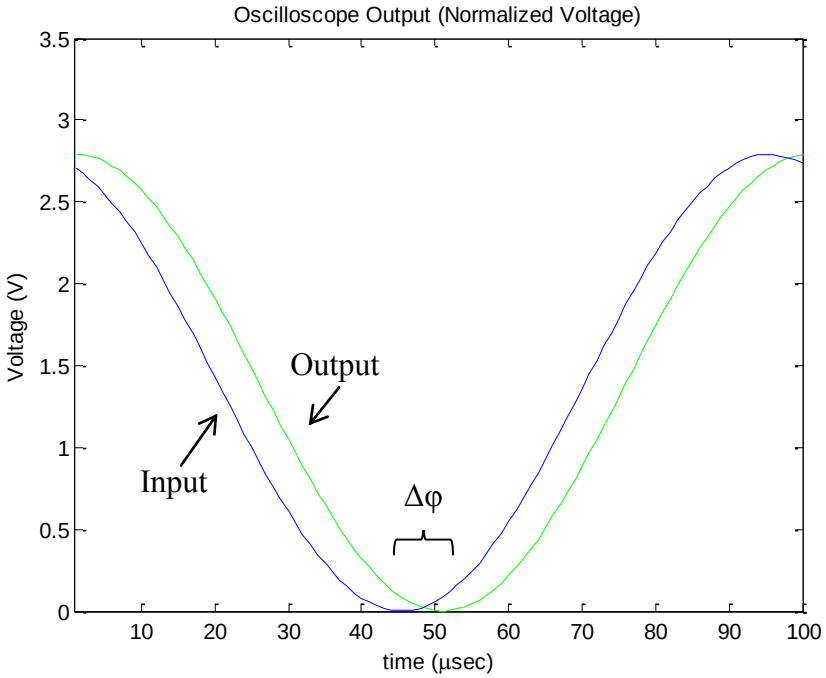


**Figure 26: Oscilloscope Output Waveform**

The phase difference Δφ of 2.2 µs was converted to a capacitance value by equation (5-2) [24]:

$$C = \frac{\sin(\Delta\varphi)}{2\pi f}\frac{\tilde{v}_{res}}{R_m\tilde{v}_{cell}} \tag{5-2}$$

Referring to equation (5-2) above, $\tilde{v}_{res}$ is the magnitude of the voltage across the series resistor, $R_m$ is the series resistance value, and $\tilde{v}_{cell}$ is the magnitude voltage across the solar cell. With a forward bias of -6.6 V and a phase difference of 2.2 μs, the capacitance of the solar cell was measured to be 174.3 nF, a reasonable value for diode capacitance. To verify the accuracy and validity of this test, the same measurements were taken with zero applied voltage, and the capacitance measured from the phase shift method was identical to the multimeter value of 500.4 nF, adding faith and reliability to this method.

With two capacitance values at two different applied voltages, the doping concentrations could be investigated.

**5.2 Donor and Acceptor Doping Concentrations**

The equation for capacitance of a PN-junction reveals an obvious dependence upon doping [12].

$$C = \sqrt{\frac{q\epsilon_s N_a N_d}{2(\frac{kT}{q}\ln\left(\frac{N_a N_d}{{n_i}^2}\right) + V_R)\,(N_a + N_d)}} \tag{5-3}$$

This relationship can also be expressed in terms of products *P* and sums *S* of doping concentrations.

$$C = \sqrt{\frac{q\epsilon_s P}{2(\frac{kT}{q}\ln\left(\frac{P}{{n_i}^2}\right) + V_R)(S)}} \tag{5-4}$$

The latter form lends itself well to numerical analysis, given the preceding CV-test measurements. Since two capacitance values were measured at two different values of $V_R$, a system of two equations with two unknowns can be solved for $P$ and $S$.

$$C_1 = \sqrt{\frac{q\epsilon_s P}{2(\frac{kT}{q}\ln\left(\frac{P}{{n_i}^2}\right) + V_{R1})(S)}} \tag{5-5}$$

$$C_2 = \sqrt{\frac{q\epsilon_s P}{2(\frac{kT}{q}\ln\left(\frac{P}{{n_i}^2}\right) + V_{R2})(S)}} \tag{5-6}$$

The system of non-linear equations was solved directly in MATLAB for $P$ and $S$ yielding a value of approximately $2 \times 10^{32}$ for $P$ and $3.2 \times 10^{16}$ for $S$. Given that the product of the doping values was so much larger than the sum, it was inferred that the impurity doping of the test cell was approximately equal on each side of the PN-junction, with an approximate magnitude of $1.7 \times 10^{16}$ cm$^{-3}$.

### 5.3 Reverse Saturation Current Calculation

The impurity concentration profile of the device reveals other useful information concerning the physical properties of the PN-junction solar cell. The ideal reverse saturation current $I_s$ (dark current) is related to the doping concentrations for a short base n-side and long base p-side PN-junction by the following equation [10]:

$$I_s = \left[\frac{qD_n\frac{{n_i}^2}{N_a}}{L_n} + \frac{qD_p\frac{{n_i}^2}{N_d}}{W_b}\right]A \tag{5-7}$$

However, the width of the n-side $W_b$ is still unknown, so the reverse saturation current must be solved another way. The reverse saturation current is related to the

applied voltage across the cell, along with the total current through the cell by the following equation:

$$V_a = \ln\left(\frac{I_t}{I_s} + 1\right)\frac{kT}{q} \tag{5-8}$$

In the equation above, $I_t$ is the total current through the cell and $V_a$ is the external voltage applied across the cell. Ideally, $I_s$ remains constant with changes in applied voltage and current; therefore, if voltage and current is known the reverse saturation current can also be found. A simple circuit was devised to evaluate this test condition, in which the solar cell was placed in series with a 5 V DC source and variable resistor R1.

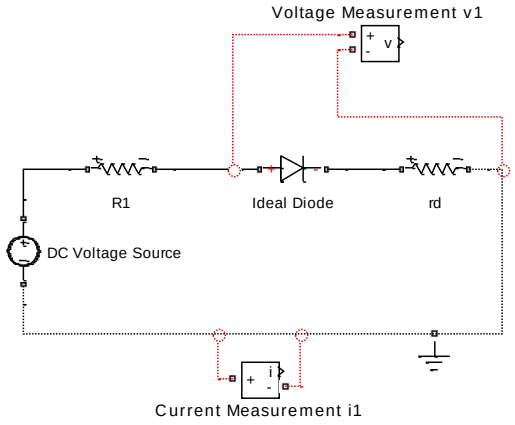


**Figure 27: Reverse Saturation Current Test Diagram**

The total current through and voltage across the cell is easily measured with a multimeter since the cell is in series with everything else in the circuit. However, there are two unknowns in the circuit shown: internal resistance $r_d$ and the voltage drop only across the ideal diode. The voltage $v_1$ measured with the multimeter includes the voltage drop across the internal resistance, but in order to fully investigate the physical properties of the cell, especially the reverse saturation current, the voltage $v_a$ must be determined since there is a observable relationship between $v_a$ and $I_s$.

$$v_1 = v_{a1} + i_1 r_d \tag{5-9}$$

$$v_{a1} = \ln\left(\frac{i_1}{I_s} + 1\right)\frac{kT}{q} \tag{5-10}$$

Since there are two unknown values $I_s$ and $r_d$, the current and voltage in the circuit must be measured twice, for two different applied voltages, so that two equations with two unknowns can be solved.

$$v_1 = \ln\left(\frac{i_1}{I_s} + 1\right)\frac{kT}{q} + i_1 r_d \tag{5-11}$$

$$v_2 = \ln\left(\frac{i_2}{I_s} + 1\right)\frac{kT}{q} + i_2 r_d \tag{5-12}$$

The reverse saturation current term must be iteratively solved using the Monte Carlo method for two different applied voltages and corresponding currents to minimize the measurement error. Using the Monte Carlo method and the test circuit described, the reverse saturation current density was determined to be approximately 6.269 pA/cm$^2$. The value for resistance $r_d$ from this method proves incomplete, however. What the quantity $r_d$ physically represents is the internal resistance of the solar cell, but the value $r_d$ measured in the preceding analysis includes the resistance of the wires and contacts, a significant contribution to error when typical diode resistance values are considered. Therefore, the precise value of diode resistance must be determined another way.

### 5.4 N/P-side Thickness Determination

In order to evaluate the test solar cell internal resistance, the n-side and p-side thicknesses of the PN-junction must be further investigated. The total thickness of the cell was measured using the scanning electron microscope (SEM).

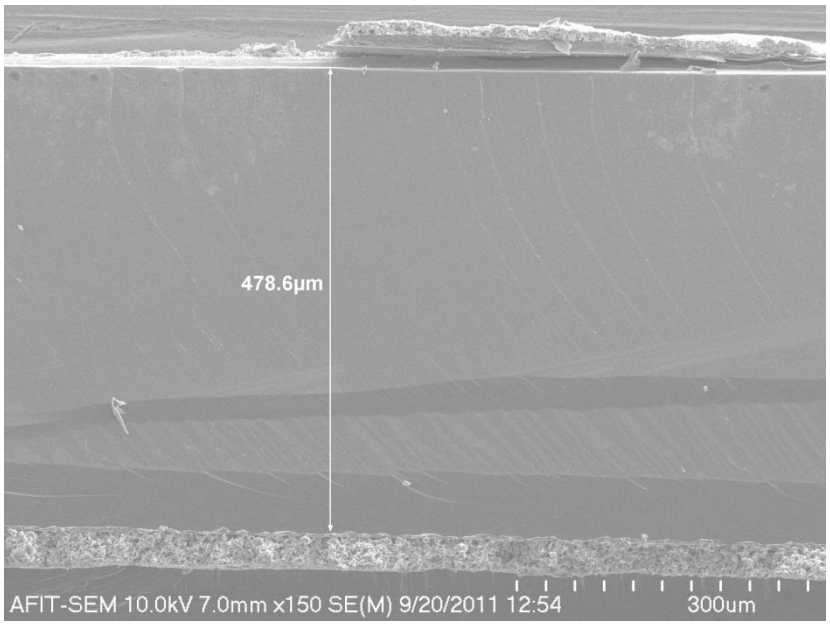


Figure 28: SEM Image of the Test Cell

Since the reverse saturation current density of the cell was solved in the previous characterization, the width of the n-side $W_b$ can be explicitly solved.

$$W_b = \frac{D_p}{N_d}\left(\frac{J_0}{qn_i{}^2} - \frac{D_n}{N_a L_n}\right)^{-1} \tag{5-13}$$

Using known values characterized in the previous analysis, the width of the n-side of the test solar cell was determined to be 40.7 µm. Given the n-side thickness, depletion region thickness ($x_b + |x_p|$), and total cell thickness, the p-side thickness can easily be solved. The p-side thickness of the test solar cell was determined to be 435.6 µm.

## 5.5 Solar Cell Internal Resistance

The internal resistance $r_d$ of a PN-junction diode is described by the following equation [12]:

$$r_d = \frac{1}{A}\left[\rho_n th_n + \rho_p th_p\right] \tag{5-14}$$

Equation (5-14) is an applied form of the familiar equation for resistance $\frac{\rho L}{A}$. The n-side and p-side thicknesses are described by $th_n$ and $th_p$ respectively, while $\rho_n$ and $\rho_p$ describe the resistivities (as a function of doping) of both regions of the cell. The internal resistance of an ideal diode is usually so low that it cannot be measured with a multimeter. Therefore, the only way to determine diode resistance is to solve the equation above. The depletion region can be neglected in the calculations because it is so small relative to the quasi-neutral regions of the solar cell. The internal resistance of the solar cell used during testing was determined to be approximately 2.8 mΩ.

### 5.6 Illumination Test Calibration

A tungsten-filament halogen lamp was used for the duration of illumination testing. An important issue encountered during any indoor solar cell test is the irradiance spectrum mismatch between the manufactured light source and the sun. A comparison of the AM 1.5 spectrum and the tungsten lamp spectrum is shown in Figure 29. Using the reference cell to calibrate the light source, the known short circuit current was reached for 1 sun. Under this lighting condition, a short circuit current of 253.9 mA was measured for the test cell.

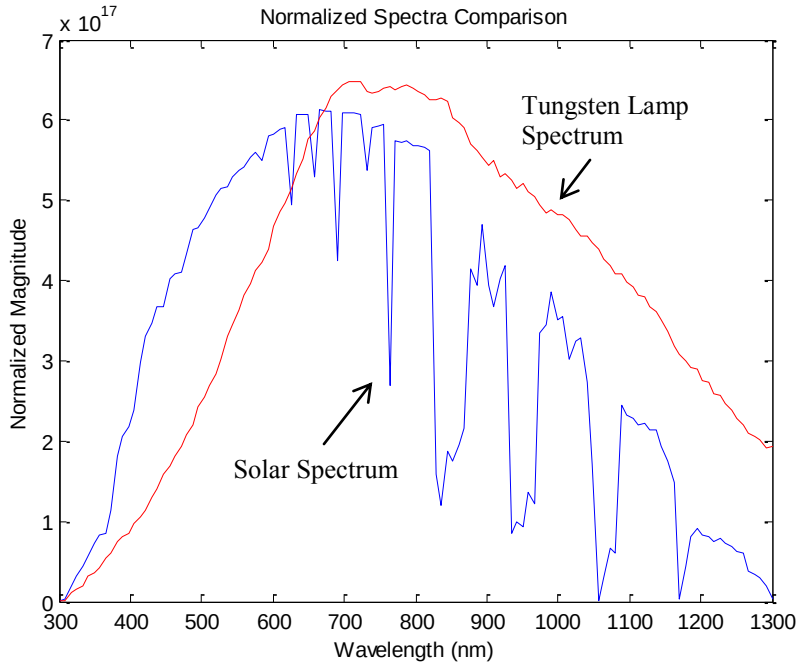


**Figure 29: Spectra Mismatch [26]**

No light source available exactly matches the spectral irradiance pattern of the sun, so in order to maximize the accuracy of the dynamic thermal model a scaling factor must be found that relates the light source spectrum to the ideal solar irradiance spectrum.

## VI: Illumination Testing

After characterizing the physical properties of the test solar cell, the steady state temperature under various concentrations was measured.

### 6.1 Test Set-up

The cell was illuminated using 150 Watt tungsten halogen lamps. A small electric fan provided a laminar flow cooling stream across the surface of the cell. The temperature of the cell was measured using a thermal couple soldered to the cell. A second multimeter was used to measure the short circuit current to determine the concentration ratio incident on the test cell, given that short circuit current is linearly dependent on concentration and changes relatively minimally with increasing temperature. A diagram of the test set-up is shown in Figure 30.

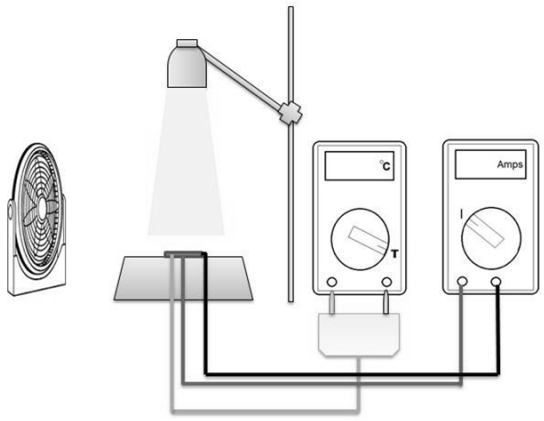


Figure 30: Illumination Test Set-up

However, before the testing could begin the thermal plate convective cooling properties of the cell were measured to determine the value for $h_{plate}$, to include in the computer model.

## 6.2 Cooling Coefficient Calibration

The convective cooling coefficient term $h_{plate}$ was introduced in the previous chapter, and is a fundamental component of the thermal model. Since the convective cooling properties depend on the airflow rate over the solar cell surface, $h_{plate}$ must be calculated for the laboratory test condition fan speed in order to maximize control in the experiment. The convective cooling coefficient given in equation (6-1) is a function of the specific heat of the solar cell material $h_{sil}$ (Silicon) and the measured exponential cooling rate of the cell $\tau_{h.}$ An extensive derivation of equation (6-1) is given in Appendix B.

$$h_{plate} = \frac{h_{sil}}{\tau_h} \tag{6-1}$$

To investigate the parameter $h_{plate}$, the cell was heated up to above the steady state temperature for one sun, and then the light source was turned off. The temperature of the cell was recorded with time as soon as the light source was turned off, essentially measuring the time back to room temperature for the cell. Plotting the temperature of the cell as a function of time the exponential form of convective cooling is revealed and can be modeled by equation (6-2).

$$T(t) = T_n e^{-\frac{t}{\tau_h}} \tag{6-2}$$

In equation (6-2) $T(t)$ is the temperature as a function of time in the convective cooling experiment, $T_n$ is the normalized maximum temperature, $t$ is time, and $\tau_h$ is the cooling rate. The temperature was plotted as a function of time for the maximum fan speed in order to measure $\tau_h$.

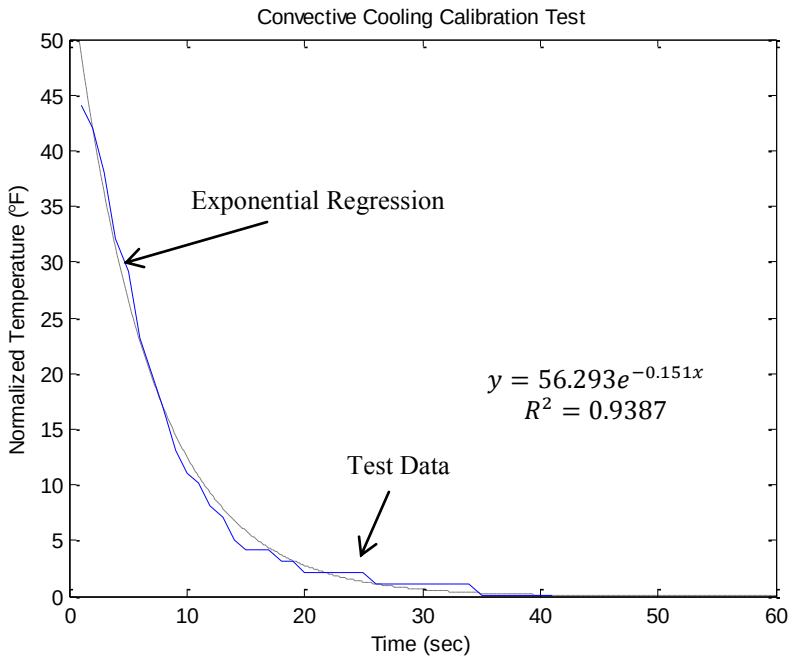


**Figure 31: Convective Cooling Calibration**

Referring to the graph shown in Figure 31, the $\tau_h$ is 6.623 from the equation of the exponential regression. The convective cooling coefficient $h_{plate}$ can then be found using equation (6-1), and the convective cooling part of the model is complete. As an addendum, $\tau_h$ for five different fan speeds in measured in Appendix C. Furthermore, a trend plot of $h_{plate}$ as a function of fan speed is given in order to investigate the importance of flow rate to the convective cooling properties of the cell.

A MATLAB plot shows the extrapolated data points demonstrating higher fan speeds than were tested in the lab in Figure 32.

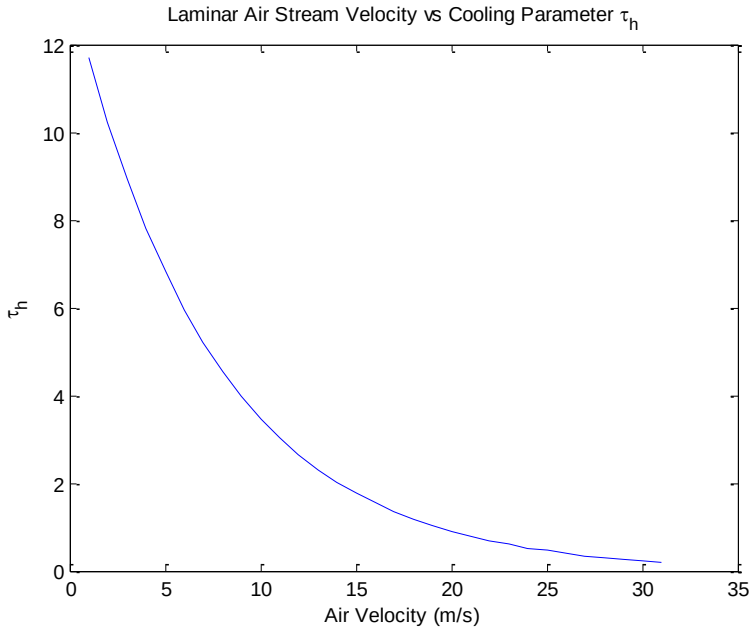


**Figure 32: MATLAB Plot of Extrapolated Cooling Parameter Values**

Obviously, as the fan speed increases the cooling coefficient $h_{plate}$ increases (eq. 6-1, 6-2) along with the effective cooling of the cell. However, a higher fan speed requires more power in order to run the fan, resulting in an optimization problem concerning both cooling and power requirements. This issue presents an opportunity for future research in this area. After the convective cooling coefficient of the cell was characterized, testing under various concentration ratios commenced.

## 6.3 Test Procedures

The illumination testing procedures were relatively straightforward. There were three steps used throughout testing to repeatedly measure steady state temperature of the cell under different illumination conditions:

1. *Measure the short circuit current ($I_{sc}$) at one sun*
2. *Use the measured $I_{sc}$ to determine different concentration ratios; increase the intensity of the light sources accordingly to reach desired concentration conditions*

3. *Record the steady state temperature for different concentration ratios*

Following the three steps described, the steady state temperature of the test cell was measured as a function of the concentration ratio.

## 6.4 Steady State Temperature Measurements

Figure 33 shows the theoretically predicted and experimentally measured steady state cell temperature as a function of concentration ratio. A strong agreement is observed between the two, where the exponential concentration ratio was limited to four suns due to limitations of the cell under test.

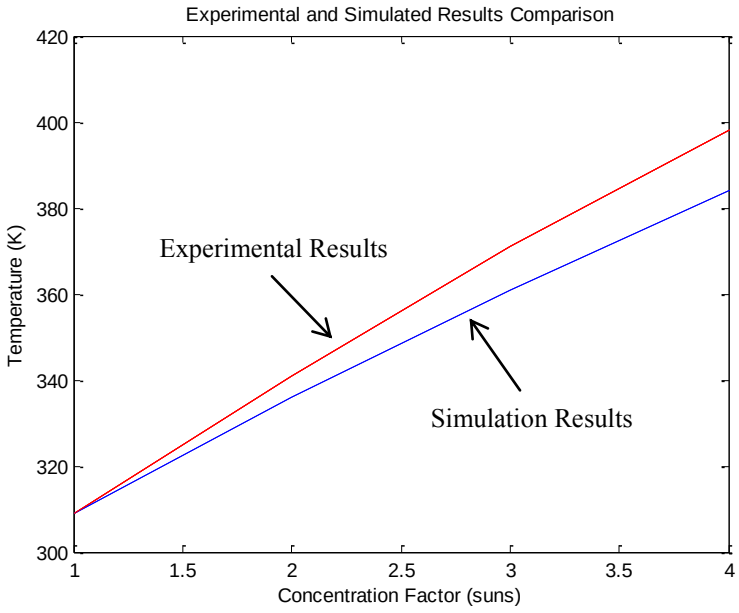


**Figure 33: Illumination Test**

The maximum steady state cell temperature measured was 398 K (257 °F), at a concentration factor of four suns. Any further increase in light intensity resulted in temperatures that compromised the test set-up and damaged the test-cell.

# VII: Simulation Results and Analysis

## 7.1 Simulation Predictions

To predict the steady state temperature of the cell as a function of concentration, the thermal model was run for different values of concentration and the temperature was calculated. Figure 34 shows a MATLAB plot of steady state temperature predictions as a function of concentration up to 35 suns.

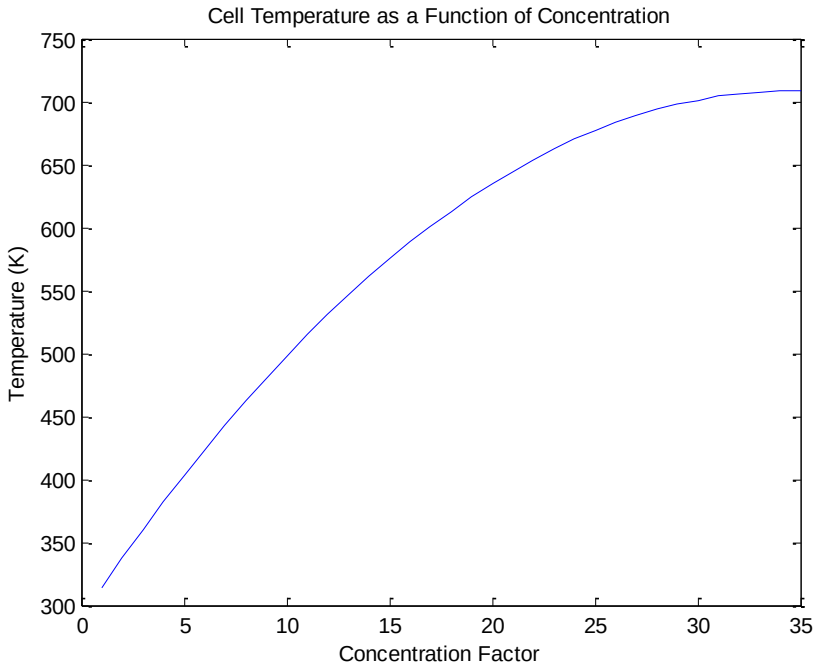


**Figure 34: Predicted Cell Temperature as a Function of Concentration**

It is interesting to note that at a concentration of 35 suns and temperature of 720 K the intrinsic carrier concentration $n_i$ for silicon is $3.8 \times 10^{16}$ /cm$^{-3}$, approaching the impurity doping levels measured from the test cell: $N_A$ and $N_D \approx 1.7 \times 10^{17}$. From a purely theoretical perspective, the simulated cell appears to violate the condition of low-level injection near 30 suns of concentration.

## 7.2 Effect of Temperature on the Electrical Properties

The thermal model developed in MATLAB provides a tangible demonstration of the severe effects an increase in temperature has on solar cell operation. As the solar cell heats up under concentration, the open-circuit voltage suffers while the short circuit current increases linearly, effectively changing the shape of the IV-curve as the concentration is increased. Figure 35 shows modeled IV-curves for various concentration ratios, where the theoretically predicted steady state cell temperature is incorporated. For each case, an impedance matched load is assumed, maximizing the fill factor and power delivered by the cell.

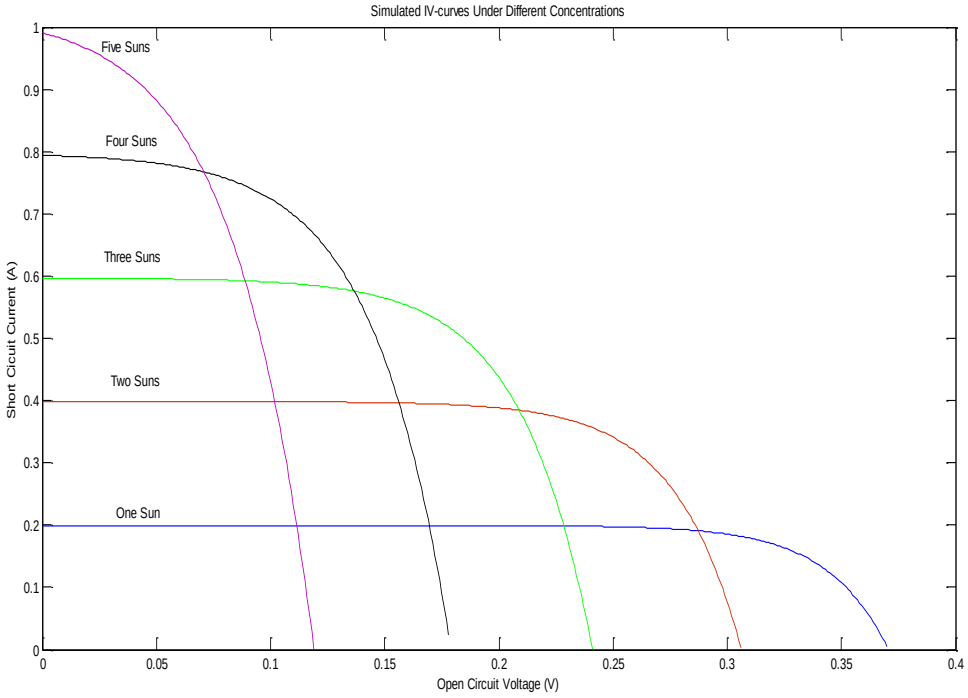


Figure 35: IV Curves for 5 Different Concentration Ratios

First order models for concentrated solar cells, not accounting for changes in temperature, presume a simple linear relationship between concentration ratio and power

output. However, as shown in Figure 35, changes in temperature have drastic effects on the maximum power output of the cell. Ideally, a CSP system should have a sufficient cooling system to keep the open-circuit voltage high even under high concentration ratios. However, the lab set-up demonstrates that the cooling system used was largely ineffective at removing enough heat to keep the open circuit voltage from collapsing under concentration. The fundamental dependence of the open circuit voltage upon temperature presents an important future research opportunity in better solar cell cooling methods.

### 7.3 Optimum Concentration Factor Analysis

Using the multiparameter approach described, the optimum concentration factor of a CSP system by incorporating the thermal effects of increased illumination into the electrical model of solar cell operation. The predicted optimum concentration for the cell used in the test set-up is plotted in Figure 36, where it was determined that 2.9 suns was the optimum concentration factor for the solar cell used in the test-set up.

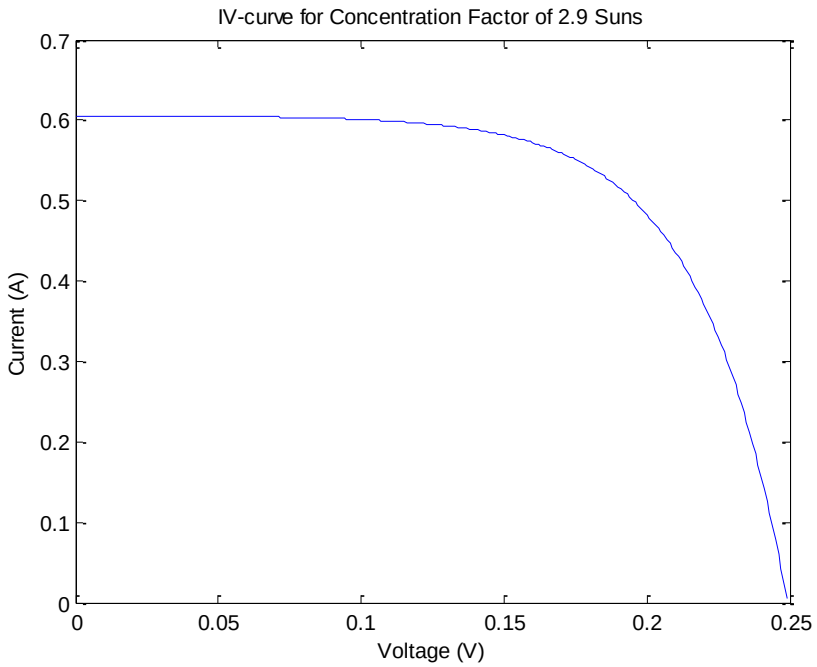


**Figure 36: IV-curve for Optimum Concentration**

Given the cooling system and cell material, any higher concentration ratios would degrade the output of the cell due to the collapse of the open circuit voltage, despite the increase in light intensity. This is a very interesting conclusion because most commercial CSP systems use concentration ratios on the order of hundreds of suns. Therefore, it can be concluded that commercial polysilicon cells are not suitable to handle high concentration ratios unless cooled extremely well. This fact also sheds light on the proprietary cooling systems used in many state-of-the-art CSP arrays. These manufacturers are using a more effective cooling system than an air fan to manage thermal runaway in these cells. Furthermore, high-efficiency solar cells are inherently better at managing heat since a higher percentage of the incident photon energy is converted to electricity.

# VIII: Conclusions

## 8.1 Discussion

This research has demonstrated the ability to predict the steady state temperature of a concentrated solar cell. Furthermore, the optimum concentration factor for the test cell was determined from simulation. The test results combined with simulated predictions revealed that the optimum concentration factor for the test set-up was much lower than hypothesized, due to the significant amount of heat contributed by multiple suns.

A novel model was developed to facilitate the computer simulation of the cell under concentration, and the model was shown to accurately predict the steady state temperature of the cell at a concentration of up to four suns. When used to predict the steady state operating temperature of the cell, the Gamma Model outperforms the other electrical solar cell models discussed in Chapter II as shown in Figure 37.

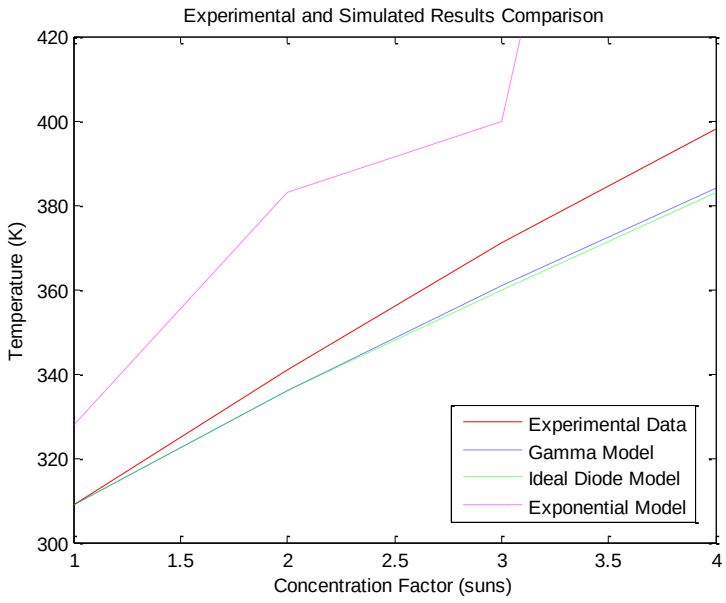


Figure 37: Electrical Model Results Comparison

Although the electrical portion of the model provides a relatively minor component of heat generated in the cell, using the wrong model (i.e. exponential model) can adversely affect the steady state temperature predictions. Furthermore, the expression for total current calculated using the Gamma Model captures the important phenomenon of surface carrier recombination, discussed in Section 2.8. This can be seen when the calculated photocurrent is compared to the current computed using the ideal diode model against the measured short circuit current of the cell, shown in Figure 38.

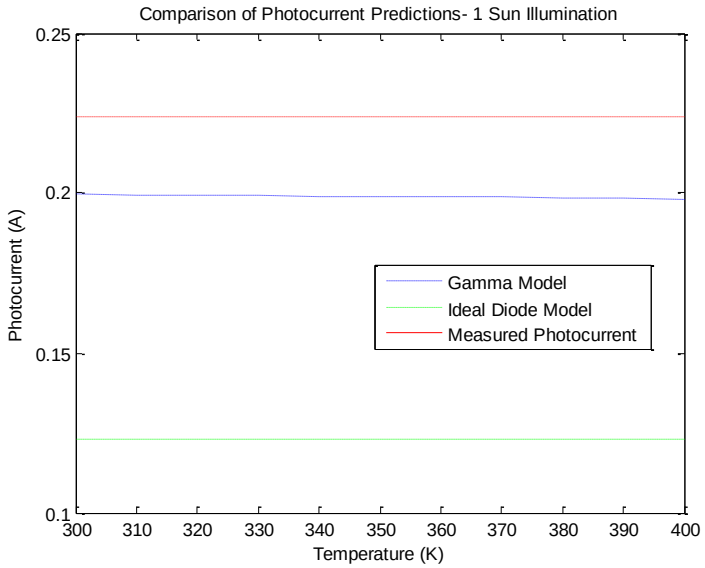


**Figure 38: Simulated Photocurrent Comparison**

The standard diode model photocurrent $I_{ph} = qG_oA(L_n + W + L_p)$, fails to adequately capture the effect of surface recombination because the assumption is made that the majority of EHP generation takes place within or near the space charge region [17], when in fact a significant amount of carrier generation takes place in the absorption layer of the device [8].

Another benefit of the Gamma Model is that the temperature dependence of the photocurrent is incorporated into the overall current calculation. Figure 39 demonstrates this contributing feature of using the Gamma Model in the solution for the solar cell current equation, showing that as the temperature of the cell increases the photocurrent decreases because of an increase in the kinetic energy within the semiconductor crystal lattice. An inclusion of the thermal effects into the electrical model yields a more complete solution for the dynamic thermal effects of the solar cell over the ideal diode model, which assumes that the photocurrent is independent of changes in temperature [17] [12].

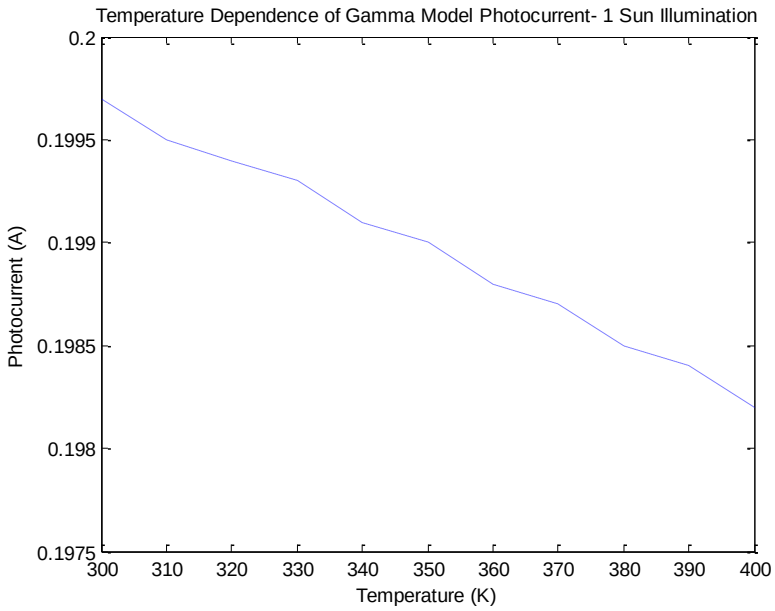


**Figure 39: Temperature Dependence Feature of Gamma Model**

Using the Gamma Model simulation, an optimum concentration factor analysis reveals that an illumination level of 2.9 suns is the best configuration for the solar cell and cooling system combination used in this research. A higher concentration factor (more suns) contributes more heat, and as the concentration factor exceeds three suns, the

open circuit voltage begins to collapse and the output efficiency decreases. Given the test cell and cooling system, it is not practical to concentrate beyond a few suns. This research has really demonstrated the importance of thermal management in a CSP system.

### 8.2 Key Contributions

There are several contributions of this research to current and future solar energy research projects. The thermal model presented in this work represents the first and only solar cell model that incorporates both the electrical characteristics and thermal properties of the cell in order to predict the steady state temperature under illumination. Thermal models developed from a purely thermodynamic perspective were studied and used in this research, but nowhere in the literature had someone combined the thermodynamic properties of the solar cell surface with the solid-state physics governing the flow of charge across the PN-junction. This research, and the Gamma Model in particular, is beneficial to future research since different materials can easily be incorporated into the computer model.

Another important contribution of this research is the novel model for excess carrier concentration in a PN-junction solar cell. Existing models use an exponential or linear approximation on both sides of the PN-junction, but upon further investigation it was determined that a more accurate model capturing the effect of surface carrier recombination was necessary to complete this research. Furthermore, it was determined that a negative exponential approximation of carrier concentration produced a mathematical singularity as the photon penetration depth approached the minority carrier

diffusion length. Using a gamma function to solve the second order different transport equation on the n-side yielded an initially complex solution that, when simplified, resulted in an eloquent solution to carrier concentration. The model was verified with experimental results that demonstrate the ability of the thermal model to predict steady state temperature as a function of concentration. The model can easily be adapted to reflect different cooling systems and with little manipulation other semiconductor materials. However, the full extent of these possibilities exceeded the boundary of this initial research.

### 8.3 Future Research

One of the main goals of this research was to open the door for future photovoltaic research at AFIT. As the first modern solar power related research project at AFIT, this work has laid the foundation for several future research opportunities in the field of solar energy.

A very exciting opportunity lies in the development of low-power methods to cool CSP systems. As was shown in this research, even a modest increase in concentration causes a severe increase of temperature that ultimately degrades the output efficiency of the cell. Passive cooling methods such as heat sinks are readily available to dissipate some of the heat, but at high concentration ratios the relative size of the heat sinks would physically dwarf the cells, essentially making them infeasible in this capacity as power-to-weight ratios are considered. A real breakthrough lies in the discovery of an efficient passive cooling system that requires no external power and effectively manages the cell temperature to an optimum operating condition. The goal of any solar power system

should be a stand-alone power supply that is optimized under every illumination condition.

The test set-up used in this research demonstrated that the active cooling system used was effective at cooling the cell, but only under low concentration ratios. Additionally, air was used as the laminar fluid in this research, but it would be very interesting to investigate the possibility of using a shallow liquid flowing over the surface of the cell to cool the system. A number of transparent liquid coolants exist to accomplish this research, but again this active cooling system would require external power. However, investigation of alternative solar cell cooling methods (both active and passive) would be extremely interesting and beneficial to the field of solar energy research.

Another future research opportunity lies in running the same illumination tests with different semiconductor material solar cells, such as GaAs, InGaP, CdTe, and other high-efficiency cell materials to investigate the thermal properties of higher efficiency solar cells, like the ones used in industrial CSP systems. Exotic multi-junction semiconductor cells are used in most modern CSP systems, but much of the research behind the design and implementation of these systems is proprietary.

A significant hurdle facing solar cell researchers in academia is that many breakthroughs in the field are often closely guarded "trade secrets". Obviously, if someone develops a technology that could dramatically increase efficiency and decrease cost that would create a major competitive advantage in this extremely competitive field. Consequently, the lucrative field of solar energy has created a vacuum of academic literature, especially research concerning CSP systems. It is the author's sincere belief

that solar energy research is especially important within the department of defense as the culture continues to shift towards energy awareness. As the military searches for ways to save money and increase efficiency across all sectors, defense-minded solar energy research will only catalyze this effort to reduce demand and increase energy supply.

## Appendix A: MATLAB Code

```
% this m-file computes the total current of the cell using ambipolar
% transport equations and the ideal diode law.  The currents are
derived
% from expressions for the excess minority carrier concentrations on
either
% side of the pn junction. The current will change depending on the
% illumination, temperature, what else?
h=6.626e-34;
c=3e8;
% IV curve!!!!
PD = [1.32 20.96 113.48 182.23 234.43 286.01 355.88 386.80 381.78
492.18 751.72 822.45 842.26 890.55 1077.07 1162.43 1180.61 1212.72
1180.43 1253.83 1242.28 1211.01 1244 1299 1273 1276 1277 1292 1284 1262
1261 1255 1240 1243 1233 1188 1228 1210 1200 1181 973 1173 1152 1133
974 1110 1086 1070 733 1036 1018 1003 988 860 932 923 914 407 857 843
835 817 807 793 778 217 163 249 231 255 279 529 496 585 486 448 486 500
100 116 108 155 139 374 383 424 382 383 323 344 345 284 175 2 30 67 59
240 226 220 211 211 201 199 180 161 136 2 39 72 80 72 70 64 68 62 57 53
50 31 28 24 15 2];
lam = 0.3e-6:0.01775e-6:2.5e-6;
R_vec=[.25 .245 .24 .235 .23 .225 .22 .21 .2 .19 .18 .17 .16 .15 .14
.13 .12 .11 .1 .1 .1 .1 .1 .1 .1 .1 .1 .1 .1 .1 .1 .1 .1 .1 .1 .1 .1
.1 .1 .1 .1 .1 .12 .14 .16 .18 .2 .22 .24 .26 .28 .3];
R_vec(54:124)=.3;
vv= 3e8./lam;
PDconv = PD.*1e-4;

F=PDconv./(h.*vv)  ; % compute flux from power density (124 elements,
ie wavelengths)

PDtg = [0.0427 .068 1.33 1.845 2.232 3.521 3.9 4.4 5.3 5.8 6.8 7.1 7.3
7.9 8.3 8.8 9.7 10.2 11.13 11.5 12 12.5 13.06 13.6 14.5 14.9 15.4 15.9
16.5 17.7 18.1 18.6 19.12 19.5 19.89 20.02 20.41 21.31 21.7 21.82 22.21
22.6 22.99 23.63 23.63 23.9 24 24.15 24.15 24 23.8 23.4 23.1 22.34
21.95 21.7 21.57 21.31 20.92 20.79 20.54 20.15 19.76 19.38 18.99 18.73
18.6 18.22 17.44 17.06 16.67 15.9 15.5 15.12 14.7 14.7 13.96 13.96
13.58 13.19 13.19 12.8 12.54 12.16 11.77 11.77 11.51 11.38 11.13 10.74
10.48 10.35 10.09 9.8 9.45 9.2 8.9 8.8 8.5 8.3 8.03 7.9 7.6 7.4 7.13
6.8 6.36 6.1 5.9 5.7 5.6 5.3 5.2 4.9 4.8 4.6 4.4 4.2 4 3.8 3.7 3.58 3.4
3.4];

PDtgscale=PDtg.*trapz(PD)/trapz(PDtg);

PDtgconv=PDtgscale.*1e-4;

Ftg=(PDtgconv./(h.*vv));

for T =300:1:700; % temperature in Kelvin (open circuit voltage
decreases while Isc increases as T rises)
A = 15 ; %  cell area = 1 cm^2
q = 1.619e-19; % electron charge (C)
k = 8.62e-5; % Boltzmann's constant
k1 = 1.38e-23; % Boltzmann's constant J/k
```

```
Vt = k*T; % thermal voltage = 0.0258 V

ni = 9.38e19*((T/300)^2)*exp(-6884/T) ; % source PV education "Intrin.
Carr. Conc." (for Si)

ND = 1.7e16;  % doping levels

NA = 1.7e16;

Dn = 1350*Vt/((1+(81*NA)/(NA+3.2e18))^(.5)); % diffusion coeffecient
for electrons (cm^2/s)

u_n = Dn/(k*T);

Dp = 480*Vt/((1+(350*ND)/(ND+1.05e19))^(.5)); % diffusion coeffecient
for holes (both temp dependent)

u_p = Dp/(k*T);

pno = ni^2/ND;          % initial minority carrier conc on the n-side
(function of temperature)

npo = ni^2/NA;          % initial minority carrier conc on the p-side

es = 11.7*8.85e-12 ; % relative permitivity for Si

vbi = (k*T)* log(NA*ND/ni^2) ; % built in voltage

xb = sqrt((2*es*(vbi)/q)*(NA/ND)*(1/(NA+ND))); % position of the depl
region boundary on n-side (w/ the center of the depl region as ref)

xp = sqrt((2*es*(vbi)/q)*(ND/NA)*(1/(NA+ND))); % position of the depl
region boundary on the p-side (w/ depl region center as ref)

tau_p = (12/(1+(ND/5e16)))*1e-6 ; % minority carrier lifetimes (s)

tau_n = (12/(1+(NA/5e16)))*1e-6 ; % (s)

Lp = sqrt(Dp*tau_p) ; % diffusion length (cm)

Ln = sqrt(Dn*tau_n) ; % (cm) make sure units work out

C = 3; % CONCENTRATION FACTOR!!

Eg = 1.17 - 4.73e-4*(T^2)/(T+636) ;

Eg_max = 1.1245;
vmin=Eg_max*q/h;
lambdamax=1000000*c/vmin; % 1.1034 um

dlambda=0.01775; % to get 124 elements

lambda_count=0;
Itot=zeros(1001,124);
```

```
Itot1=Itot;
Itot2=Itot;
Itot3=Itot;
Itot4=Itot;
Itot5=Itot;

for lambda=0.3:0.01775:2.5; %

    lambda_count=lambda_count+1;



R= R_vec(lambda_count); % reflectivity for Si about 20%

v=(c/lambda)*1000000;

Ftemp=dlambda*Ftg(lambda_count).*C;

l1 = 0.5;
l2 = 0.8;
l3 = 1.1;

if(lambda<l1)
alpha = 10^(-6.7*lambda+7.4); % how far photons penetrate into material
(1/cm)
  end
  if((lambda>l1)&&(lambda<l2))
alpha = 10^(-3.3*lambda+5.6);
  end
  if ((lambda>l2)&&(lambda<l3))
alpha = 10^(-6.7*lambda+8.4);
  end
  if (lambda>l3)
alpha = 0 ;
  end

  alpha=alpha; % to go from 1/m to 1/cm
alpha_vec(lambda_count)=alpha;
% alpha will vary from 10^6 - 10
pen_depth= 1./alpha_vec; % penetration depth in cm

% hv is the number of joules per photon

Go_prime = alpha*Ftemp ; % gen rate at surface photons/cm^3/s

nthick = 3e-4 ; % thickness of n-side (cm)

Go = Go_prime*exp(-(nthick-xb).*alpha)*(1-R) ;  % gen rate at edge of
depl boundary

Go_vec(lambda_count)=Go;

W=xb+abs(xp) ; % width of the depletion region

count = 0 ; % store each current in a diff count variable
```

```
if(lambda<=lambdamax)
for Va = 0:0.001:1; % this is in VOLTS

    count = count + 1;
    %if((1/(Lp^2))>alpha^2)

    Itot1(count,lambda_count)=A*(q*Dp*((pno*(exp(Va/(k*T))-
1)*exp(2*xb/Lp))/(1 -exp(2*xb/Lp))*(1/Lp)));

    Itot2(count,lambda_count)=A*(q*Dp*((pno*(exp(Va/(k*T))-1))/(1 -
exp(2*xb/Lp))*(1/Lp)));
    Itot3(count,lambda_count)=A*q*Dp*((Go.*(1/alpha+(nthick-
xb))./(2*Dp)); %new photo current
    %Itot3(count,lambda_count)=A*q*Dp*(alpha.*Go./(Dp*(1/(Lp^2)-
alpha^2))); %photo current flows in the reverse bias direction (opposi
    Itot4(count,lambda_count)=-A*q*Dn*(npo*(exp(Va/(k*T))-
1)*exp(xp/Ln)*1/Ln);
    %end
%Itot5(count,lambda_count)=A*Go*q*.01 ; % any photon that makes it to
the depletion region gets turned into a carrier
Itot5(count,lambda_count)=(Go_prime./alpha)*A*q*(exp(-nthick+xb)-exp(-
nthick-xp));
    Itot(count,lambda_count)
=Itot1(count,lambda_count)+Itot2(count,lambda_count)+Itot3(count,lambda
_count)+Itot4(count,lambda_count)+Itot5(count,lambda_count);
Vaplot(count) = Va ;

end
end
end

Itot22=sum(Itot,2);
hold on
P = Vaplot.*Itot22';  %
xx=find(P>=0);
if (T == 361);
plot(Vaplot(xx),Itot22(xx));
end
maxpowercount = find(P == max(P));

Iop(T-299) = Itot22(maxpowercount) ; % operating current for max power


%%  This subroutine m-file computes the entire time dependent component
of
% heat generated by the cell under illumination.  In order to reach
steady
% state, the amount of heat generated by the cell must eventually be
% balanced out by the amount of heat dissipated by the cell

n0 =  (ND-NA)/2 + sqrt(((ND-NA)/2)^2+ni^2) ; % ni^2 = n*p ;  NA+n =
ND+p

p0 = ni^2/n0 ;
```

```
sigma = q*(n0*u_n+p0*u_p) ;% mobility of both holes and electrons
DECREASES with increasing temp!

rho= 1/sigma ; % sigma is conductivity, increases with temp increase

W= 1 ; % cm
L= 1 ; % cm

pthick = .06 ; % thickness in cm

t= 470e-6 ;  % total cell thickness

%Rcell = rho*L/(W*t) ; % ohm-cm sheet resistance
Rcell = .10; % ohms
Pr= Iop(T-299)^2*Rcell ; % heat due to illumination (Itot computed in
another subroutine)


Eg = 1.17 - 4.73e-4*(T^2)/(T+636) ; % source
http://www.ioffe.rssi.ru/SVA/NSM/Semicond/Si/bandstr.html

lambda_count2=0;

%  this is for photons ABOVE bg energy

for lambda3 = 0.3:0.01775:lambdamax;
    lambda_count2=lambda_count2+1;
    R=R_vec(lambda_count2);
    Ftemp=dlambda*Ftg(lambda_count2).*C;


    vv2=(c/lambda3)*1000000;
    Pa2(lambda_count2)=(A).*(((h*(vv2)/q)-Eg)*q*(1-R).*(Ftemp));
end
for lambda2=lambdamax+.01775:.01775:2.5; % 1.1034 is lambdamax (140
data pts)

   lambda_count2=lambda_count2+1;
   R=R_vec(lambda_count2);
    Ftemp=dlambda*Ftg(lambda_count2).*C;

    vv=(c/lambda2)*1000000;
   %Pa2(lambda_count2)= (A)*(h*c/lambda2)*(Ftemp)*(1-R) ;
% accounts for temp change F= flux (J/sec)! increases as temp rises
since the band gap decreases
Pa2(lambda_count2)= (A).*(((h*(vv)/q))*q*(1-R).*(Ftemp));
end

%Pa_tot=sum(Pa2)+sum(Pa);
Pa_tot=sum(Pa2);

Pgen = Pr + Pa_tot ;
%Pgen= Pa_tot;
%% 19 July 2011
% This subroutine m-file computes the time dependent amount of heat
```

```
% dissipated from the solar cell under illumination


sigma = 5.6704e-8  ; %  W/(m^2*K^4)

Pbb = (A)*.0001*sigma*(T^4); % blackbody radiation (convert area to
m^2)

Tstream = 300 ;

Hsil=0.0123;

%tau_H=9.259; % 1.75 m/s (slowest setting on the POT)

tau_H=6.625; % 4.25 m/s (fastest setting on POT)

%tau_H=1; % example

hplate = Hsil/tau_H  ;

Pc = hplate*(A)*(T-Tstream) ;% convective cooling of the cell by the
ambient air

% as it stands now, Pc remains constant with temp (could be refined to
% reflect changes in T)

Pdiss = Pbb + Pc ; % total heat dissipated from the solar cell

%%

Ptot(T-299) = Pgen - Pdiss ;
end
Ptot2=abs(Ptot);

steadystatecount = find(Ptot2 == min(Ptot2));

steady_state_temp=steadystatecount+299
```

## Appendix B: Convective Cooling Coefficient Derivation

The expression for $H_{plate}$ shown by equation (6-1) was derived using thermodynamic steady state cooling properties. Initially, the change in temperature with respect to time $\left(\frac{dT}{dt}\right)$ is expressed in terms of the total power dissipated and the inverse of specific heat, where $H_{sil}^{-1}$ is the inverse of specific heat (for Si) and $PD$ is the total power dissipated.

$$\frac{dT}{dt} = H_{sil}{}^{-1} PD \tag{B-1}$$

The resulting dimensional analysis of (B-1) proves the validity of this expression, where temperature is in units of Kelvin $K$, time is in units of seconds, power is in units of Joules per second, and the inverse of specific heat is in units of Kelvin per Joule .

$$\left(\frac{K}{s}\right) = \left(\frac{K}{J}\right)\left(\frac{J}{s}\right) \tag{B-2}$$

As demonstrated in Chapter IV, specifically equations (4-11) and (4-12), the heat dissipated can be expressed as a function of both the convective cooling and the blackbody cooling. Additionally, the change in temperature with respect to time should be negative since the convective cooling will decrease the temperature with time. Using the full expression for power dissipated and the correct sign for the change in temperature, equation (B-1) can be more completely expressed by equation (B-3).

$$-\frac{dT}{dt} = H_{sil}{}^{-1}\left(H_{plate}(T - T_c) + \sigma(T - T_c)^4\right) \tag{B-3}$$

Equation (B-3) takes the form of an ordinary differential equation, and must be solved in order to extract an expression for temperature. Following the procedure used to solve any differential equation, a conjecture to the solution of equation (B-3) is made

using an exponential form for temperature, given by equation (B-4) where $T_m$ is the maximum temperature, $T_c$ is the temperature of the convective cooling stream, and $\tau_H$ is the exponential cooling decay rate.

$$T = (T_m - T_c)e^{-\frac{t}{\tau_H}} + T_c \tag{B-4}$$

Referring to equation (B-4), at $t = 0$ the light source is turned off, and at $t = \infty$ the steady state temperature point is reached and the temperature is equal to $T_c$. The solution conjecture given by (B-4) must be used in the original differential equation to determine its validity as a solution.

$$e^{-\frac{t}{\tau_H}}\left(\frac{T_m - T_c}{\tau_H}\right) = {H_{sil}}^{-1}H_{plate}(T_m - T_c)e^{-\frac{t}{\tau_H}} + {H_{sil}}^{-1}\sigma(T_m - T_c)^4 e^{-\frac{4t}{\tau_H}} \tag{B-5}$$

Expression (B-5) can be simplified by removing the like exponential terms and the like temperature difference terms $(T_m - T_c)$.

$$\left(\frac{1}{\tau_H}\right) = {H_{sil}}^{-1}H_{plate} + {H_{sil}}^{-1}\sigma(T_m - T_c)^3 e^{-\frac{3t}{\tau_H}} \tag{B-6}$$

Since the goal of this analysis is to determine steady state temperature, equation (B-6) can be used to solve for $H_{plate}$ as $t \to \infty$, since the exponential term is driven to zero. The resulting solution concludes the derivation.

$$\left(\frac{1}{\tau_H}\right) = {H_{sil}}^{-1}H_{plate} \tag{B-7}$$

$$\left(\frac{H_{sil}}{\tau_H}\right) = H_{plate} \tag{B-8}$$

# Appendix C: Thermal Coefficient for Different Air Velocities

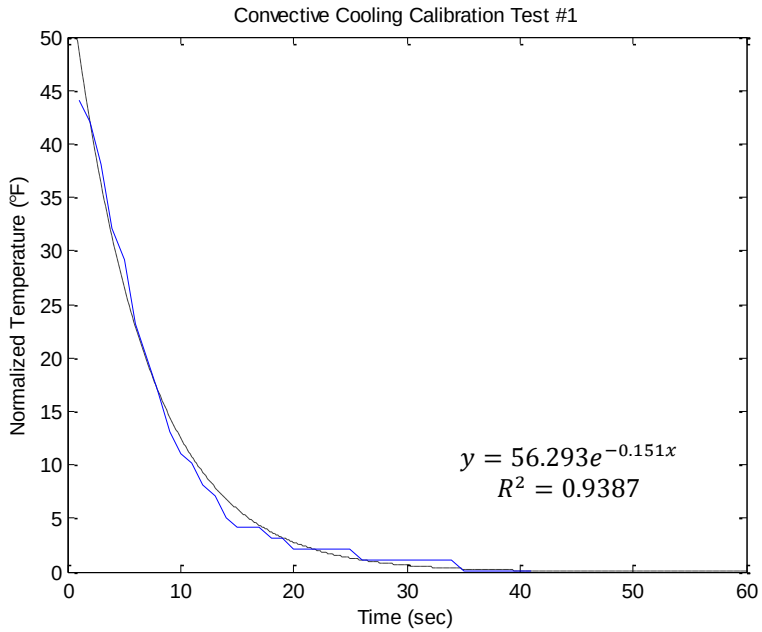


Figure 40: Cooling Coefficient test- Air Velocity 4.25 m/s

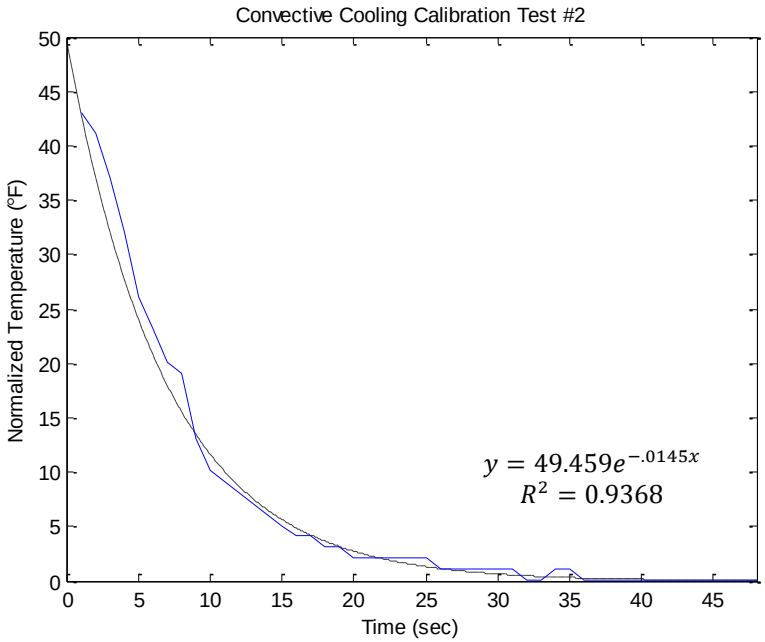


Figure 41: Cooling Coefficient Test- Air Velocity 3.75 m/s

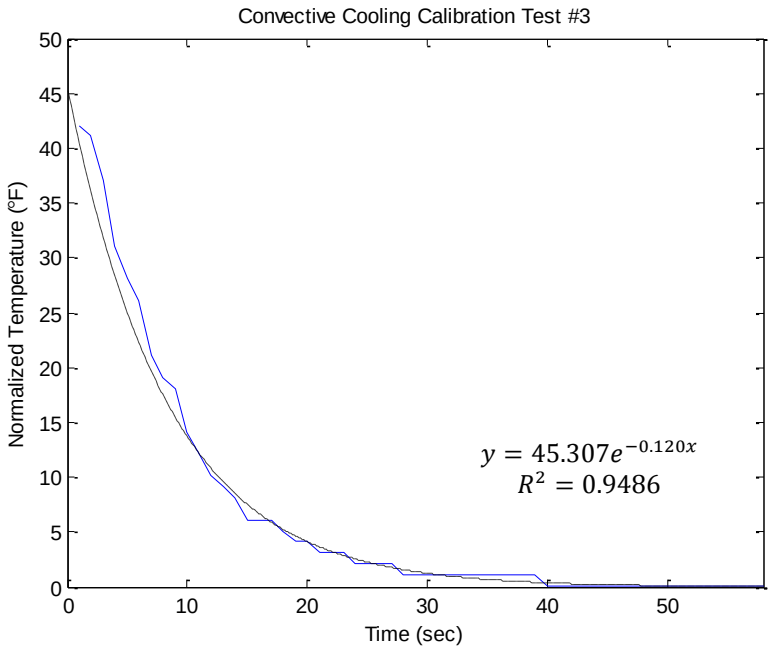


Figure 42: Cooling Coefficient Test- Air Velocity 3.0 m/s

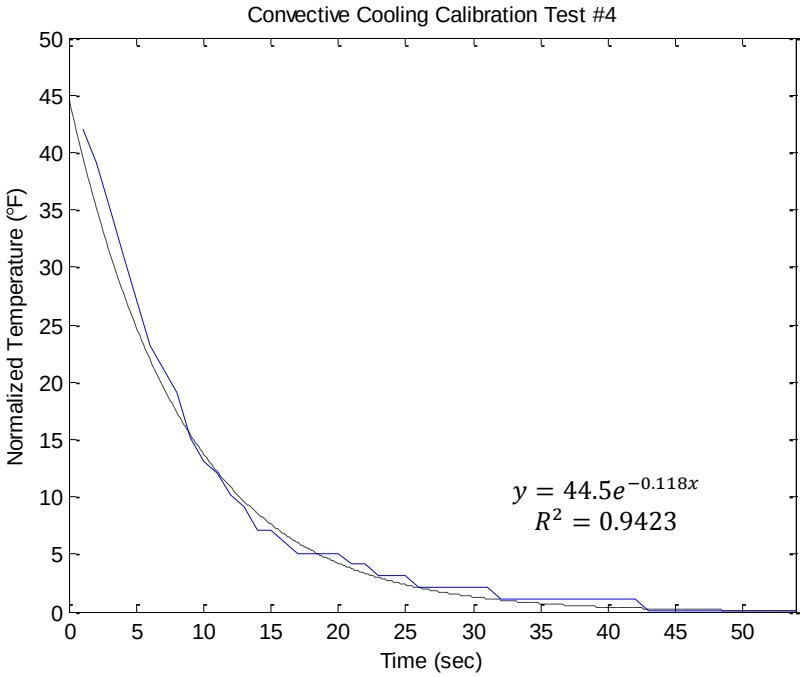


Figure 43: Cooling Coefficient Test- Air Velocity 2.25 m/s

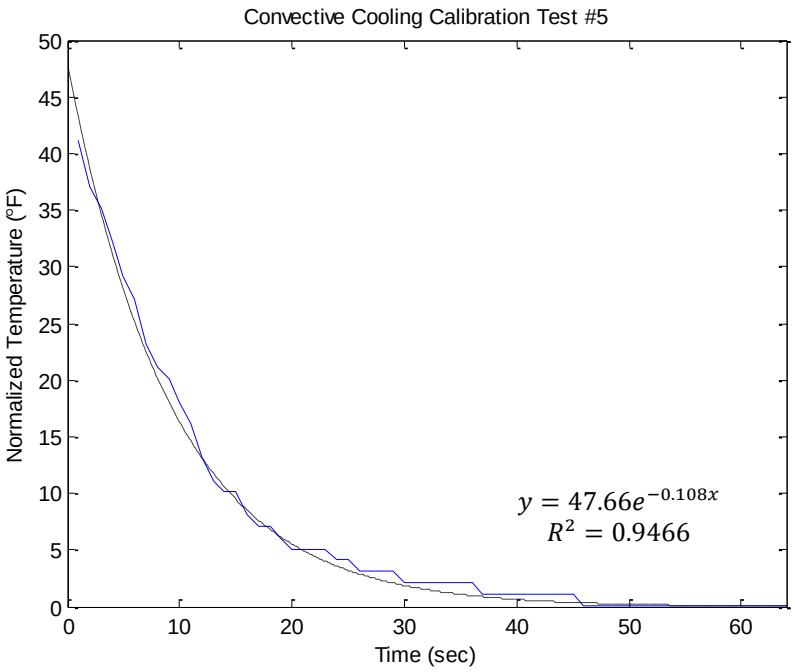


Figure 44: Cooling Coefficient Test- Air Velocity 1.75 m/s

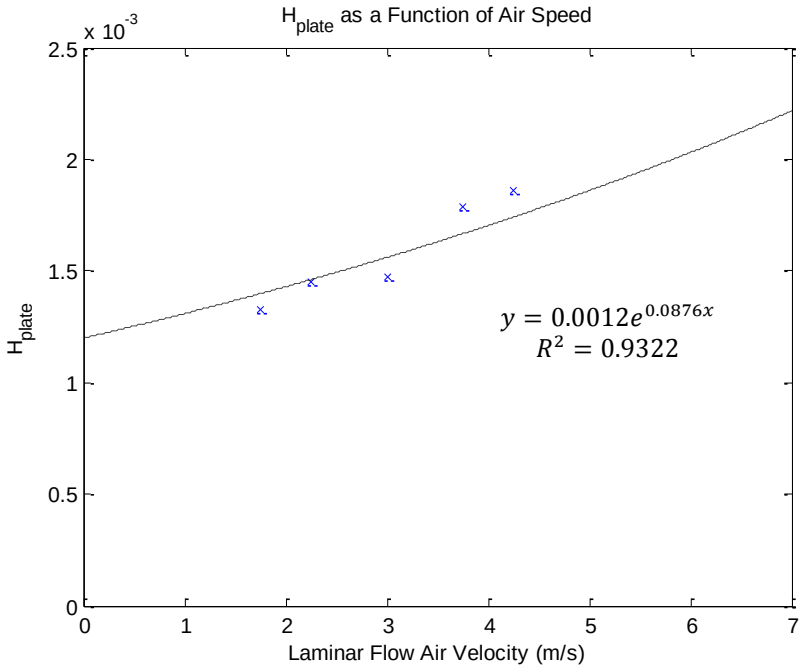


Figure 45: Hplate as a Function of Laminar Air Velocity

# Bibliography


1. *Air Force Energy Plan.* s.l. : U.S. Air Force Installations, Environment and Logistics, 2010.

2. **Doggett, Tom.** Global Energy Demand Seen Up 44 Percent by 2030. *Reuters News Agency.* [Online] 2009. http://www.reuters.com/article/2009/05/27/us-eia-global-demand-idUSN2719528620090527.

3. Annual Energy Review. *U.S. Energy Information Administration.* [Online] 2009. http://www.eia.gov/emeu/aer/pecss_diagram.html.

4. **Jokipii, J. R.** Comsicopia. *NASA Helios.* [Online] May 27, 2009. http://helios.gsfc.nasa.gov/qa_sun.html.

5. *Air Force Infastructure Energy Plan .* s.l. : U.S. Air Force, 2010.

6. **Lammers, Heather.** National Renewable Energy Laboratory. *NREL Helping Army Be as Green as it Can Be.* [Online] April 2011. http://www.nrel.gov/features/20110406_army.html.

7. **Rosenthal, Elizabeth.** U.S. Military Orders Less Dependence on Fossil Fuels. *New York Times.* 2010.

8. **Luque, Antonio.** *Solar Cells and Optics for Photovoltaic Concentration.* Philadelphia, PA : IOP Publishing, 1989.

9. ''NREL Solar Cell Sets World Effeciency Record at 40.8 Percent'. [Online] 2008. www.nrel.gov/news/press/2008/625.html.

10. **McKelvey, J. P.** *Solid State Physics for Engineering and Materials Science.* s.l. : Krieger Publishing Company, 1993.

11. Typical Range of Conductivities for Insulators, Semiconductors, and Conductors. *GlobalSino.* [Online] 2010. http://www.globalsino.com/micro/1/1micro9915.html .

12. **Neamen, Donald A.** *Semiconductor Physics and Devices.* New York : McGraw-Hill, 2003.

13. Direct and Indirect Band Gap Semiconductors. *University of Cambridge.* [Online] 2010. http://www.doitproms.ac.uk/tlplib/semiconductors/direct.php?printable=1.

14. **Muller, Richard S. and Kamins, Theodore I.** *Device Electronics for Integrated Circuits.* New York, NY : John Wiley and Sons, INC., 2003.

15. Chapter 4: PN-junctions. *University of Colorado at Boulder- Department of Electrical Engineering.* [Online] 2010. http://ecee.colorado.edu/~bart/book/book/chapter4/ch4_2.htm#4_2_2.

16. **Honsberg, Christina.** *Derivation of the Ideal Diode Equation for Photovoltaics.*

17. **Kasap, S.O.** *Optoelectronics and Photonics Principles and Practices.* Upper Saddle River, NJ : Prentice-Hall, 2001.

18. Crystalline Silicon Photovoltaic Cells. *U.S. Department of Energy.* [Online] http://www.eia.doe.gov.

19. *Comparison and Optimization of the Performance of Si and GaAs Solar Cells.* **Wong, J. Liou and W.W.** s.l. : Solar Energy Materials and Solar Cells, 1992.

20. **Moller, Hans Joachim.** *Semiconductors for Solar Cells.* s.l. : Artech House, 1993.

21. *The Limiting Effeciency of Silicon Solar Cells under Concentrated Sunlight.* **Campbell, Patrick and Martin A. Green.** 2, s.l. : IEEE Transactions on Electron Devices, 1986, Vols. ED-33.

22. *Characteristics and Performance of Silicon Solar Cells Between Low and High Level Injection Part II: Results of the Study.* **Wolf, Michael and Wolf, Martin.** 4, s.l. : IEEE, 1985, Vols. ED-32.

23. *I-V Characteristics and Performance of Silicon Solar Cells Between Low and High Level Injection Part I: The Modeling Method.* **Wolf, Michael and Wolf, Martin.** 5, s.l. : IEEE, 1984, Vols. ED-31.

24. **Fahrenbruch, Alan L.** *Fundamentals of Solar Cells: Photovoltaic Solar Energy Conversion.* New York, NY : Academic Press, 1983.

25. **Kay, Stephen.** *Intuitive Probability and Random Processes Using MATLAB.* s.l. : Springer, 2005.

26. *The Importance of Surface Recombination and Energy-Bandgap Narrowing in PN-junction Silicon Solar Cells.* **Fossum, Jerry G.** 9, s.l. : IEEE Transactions on Electron Devices, 1979, Vols. ED-26.

27. *Electric and Thermal Model for Non-Uniformly Illuminated Concentration Cells.* **Luque, Antonio, Sala, G. and Arboiro, J.C.** s.l. : Elsevier, 1998, Vol. 51.

28. Conductive Heat Tranfer. *Engineering Toolbox.* [Online] 2010. http://www.engineeringtoolbox.com/conductive-heat-transfer-d_428.html.

29. **Steel, Steve et al.** *Thermal Runaway Failures of CPV Systems.* s.l. : Semprius Corporation, 2010.

30. *Determination of the Base-Dopant Concentration of Large Area Crystalline Silicon Solar Cells.* **Hinken, David, et al.** 11, s.l. : IEEE Transactions on Electron Devices, 2010, Vol. 57.

31. Quartz Tungsten Halogen Lamps. *Newport Lighting Systems.* [Online] June 2011. http://www.newport.com/Quartz-Tungsten-Halogen-Lamps/378263/1033/info.aspx.

32. **Messenger, Robert A. and Ventre, Jerry.** *Photovoltaic Systems Engineering.* s.l. : CRC Press, 2010.

33. *Excitation of the Diffusion Length of Solar Cells from the Spectral Response of the Open-Circuit Voltage.* **Mackel, H. and Cuevas, A.** s.l. : Australian National University.

34. *A First Order Theory of the p+-n-n+ Edge Illuminated Silicon Solar Cell at Very High Injection Levels.* **Goradia, Chandra and Sater, Bernard L.** 4, s.l. : IEEE, 1977, Vols. ED-24.

35. *Performance Evaluation of Photovoltaic Silicon Cells Under Concentrated Sunlight.* **Zakzouk, A.K.M, Mujahid, A. and El-Shobokshy, M.S.** King Saud University : IEEE, 1983, Vol. E13.

36. **Zauscher, Melanie D.** *Solar Photovoltaic Panels from a Heat Transfer Perspective.* s.l. : University of California San Diego, 2006.

37. **Honsberg, Christina.** *Solar Cell Operation.* s.l. : University of Deleware, 2008.

38. **Mazer, Jeffrey A.** *Solar Cells: An Introduction to Crystalline Photovoltaic Technology.* Norwell, MA : Kluwer Academic Publishers, 1997.

39. *Model of Photovoltaic Module in MATLAB.* **Gonzalez-Longatt, Francisco M.** 2DO Congreso Iberoamericano de Estudiantes de Ingenieria Electrica, s.l. : Cibelec, 2005.

40. **Brogren, Maria.** *Optical Effeciency of Low-Concentrating Solar Energy Systems with Parabolic Reflectors.* s.l. : Universitatis Upsaliensis, 2004.

41. **Honsberg, Christina.** *Solar Electric Systems.* s.l. : University of Deleware, 2008.

42. Heat Transfer Resulting from Laminar Flow Over an Isothermal Plate. *Efunda.* [Online] Global Spec. [Cited: May 23, 2011.] http://www.efunda.com/formulae/heat_transfer/convection_forced/calc_lamflow_isothermal_plate.

43. *Photovoltaic Devices.* Hong Kong, China : Chinese University of Hong Kong, 2010.

44. *A Simple Passive Cooling Structure and its Heat Analysis for 500 X Concentration PV Module.* **Araki, Kenji, Uozumi, Hisafumi and Yamaguchi, Masafumi.** Nagoya, Japan : IEEE, 2002.

45. *The Effects of High Level Injection on the Performance of High Intensity, High Effeciency Silicon Solar Cells.* **Banghart, E. K., Gray, J. L. and Schwartz, R. J.** Purdue University : IEEE, 1988.

46. **Patel, Mukund R.** *Wind and Solar Power Systems: Design, Analysis, and Operation.* Boca Raton, FL : Taylor and Francis Group, 2006.

47. **Partain, Larry D.** *Solar Cells and Their Applications.* New York, NY : John Wiley and Sons, INC., 1995.

48. *Diffusion Length Measurement by Means of Ionizing Radiation.* **Rosenzweig, W.** s.l. : Bell System Technical Journal, 1962.

# REPORT DOCUMENTATION PAGE

*Form Approved*
*OMB No. 074-0188*



| **1. REPORT DATE** *(DD-MM-YYYY)* | **2. REPORT TYPE** | **3. DATES COVERED** *(From – To)* |
|---|---|---|
| 22-03-2012 | Master's Thesis | Oct 2010 – Mar 2012 |

**4. TITLE AND SUBTITLE**

Optimum Concentration Ratio Analysis Using Dynamic Thermal Model for Concentrated Photovoltaic System

**5a. CONTRACT NUMBER**

**5b. GRANT NUMBER**

**5c. PROGRAM ELEMENT NUMBER**

**6. AUTHOR(S)**

Avrett, John T. II, 2nd Lt, USAF

**5d. PROJECT NUMBER**

**5e. TASK NUMBER**

**5f. WORK UNIT NUMBER**

**7. PERFORMING ORGANIZATION NAMES(S) AND ADDRESS(S)**

Air Force Institute of Technology
Graduate School of Engineering and Management (AFIT/EN)
2950 Hobson Way
WPAFB OH 45433-7765

**8. PERFORMING ORGANIZATION REPORT NUMBER**

AFIT/GE/ENG/12-01

**9. SPONSORING/MONITORING AGENCY NAME(S) AND ADDRESS(ES)**

(Intentionally Left Blank)

**10. SPONSOR/MONITOR'S ACRONYM(S)**

**11. SPONSOR/MONITOR'S REPORT NUMBER(S)**

**12. DISTRIBUTION/AVAILABILITY STATEMENT**

Distribution statement A: Approved for public release; Distribution unlimited.

**13. SUPPLEMENTARY NOTES**



**14. ABSTRACT**

Concentrated photovoltaic (PV) technology represents a growing market in the field of terrestrial solar energy production. As the demand for renewable energy technologies increases, further importance is placed upon the modeling, design, and simulation of these systems. Given the U.S. Air Force cultural shift towards energy awareness and conservation, several concentrated PV systems have been installed on Air Force installations across the country. However, there has been a dearth of research within the Air Force devoted to understanding these systems in order to possibly improve the existing technologies. This research presents a new model for a simple concentrated PV system. This model accurately determines the steady state operating temperature as a function of the concentration factor for the optical part of the concentrated PV system, in order to calculate the optimum concentration that maximizes power output and efficiency. The dynamic thermal model derived is validated experimentally using a commercial polysilicon solar cell, and is shown to accurately predict the steady state temperature and facilitates computer analysis and prediction of the ideal concentration factor.

**15. SUBJECT TERMS**

Solar Cell Modeling, Photovoltaics, Concentrated Solar Power, Thermal Modeling

| **16. SECURITY CLASSIFICATION OF:** | | | **17. LIMITATION OF ABSTRACT** | **18. NUMBER OF PAGES** | **19a. NAME OF RESPONSIBLE PERSON** |
|---|---|---|---|---|---|
| **a. REPORT** | **b. ABSTRACT** | **c. THIS PAGE** | | | Dr. Stephen C. Cain (ENG) |
| U | U | U | UU | 129 | **19b. TELEPHONE NUMBER** *(Include area code)* (937) 255-3636, x4716 stephen.cain@afit.edu |